The Malvinas Current at the Confluence With the Brazil Current: Inferences From 25 Years of Mercator Ocean reanalysis

Camila Artana, Christine Provost, Jean-Michel Lellouche, Marie-Hélène Rio, Ramiro Ferrari, Nathalie Sennéchael

The Malvinas Current at the Confluence with the Brazil Current: inferences from 25 years of Mercator Ocean reanalysis.

Camila Artana[1], Christine Provost[1], Jean-Michel Lellouche[2], Marie-Hélène Rio[3], Ramiro Ferrari [4] and Nathalie Sennéchael [1]

1: Laboratoire LOCEAN-IPSL, Sorbonne Université, (UPMC, Université Paris 6), CNRS, IRD, MNHN, Paris, France

2: MERCATOR-OCEAN, Parc Technologique du Canal, Ramonville St. Agne, France

3: ESRIN-ESA, European Space Agency, Largo Galileo Galilei, 2 00044 FRASCATI, RM, Italy

4: DCAO/FCEN/UBA, CIMA/CONICET-UBA and UMI IFAECI-3351, Buenos Aires, Argentina

Key Points:

- Twenty-five years of Mercator Ocean reanalysis are examined at the Brazil Malvinas Confluence from synoptic to interannual time scales.
- The Malvinas Current branches at the Confluence: the outer part veers offshore, the inner part subducts and flows north along the slope.
- The migrations of the Subtropical and Subantarctic Fronts are large (small) at the synoptic and interannual (seasonal) time scales

Abstract

Twenty-five years of high-resolution (1/12°) ocean reanalysis are used to examine the Confluence of the Malvinas Current (MC) with the Brazil Current (BC) from synoptic to interannual time scales. The model transports of the MC (38.0 Sv ± 7.4 Sv 57 at 41°S) and the BC (23.0 Sv ± 11 Sv at 36°S) agree with observations. The model shows the branching of the MC near the Confluence with an offshore branch returning south and an inner branch sinking below the BC and managing to continue northward along the continental slope. Northward velocities associated with the subsurface inner branch peak at 40 cm/s at 36°S at 700 m depth. The model documents the migrations of the Subantarctic (SAF) and Subtropical front (STF) at the Confluence. The SAF and STF positions vary over a large range at synoptic (800 km) and interannual scale (300 and 200 km respectively) compared to the rather small seasonal migrations of the STF (150 km) and SAF (50 km). While trends in the MC are small over the 25-years of the reanalysis, the BC becomes more intense (12.5 cm/s), saltier (0.37 psu) and warmer (2.5°C) in the upper 1000 m. These trends are accompanied with a southward displacement of the STF and the SAF of 150 and 50 km.

Plain Language Summary:

The Brazil-Malvinas Confluence is a highly dynamic region. Reproducing the circulation at the Confluence is a stringent test for operational models. Mercator Ocean high-resolution (1/12°) ocean systems show remarkable performance in this region. We took advantage of twenty-five years of ocean reanalysis to examine variations in the Malvinas Current at 41°S, in the Brazil Current at 36°S and in their confluence. The Malvinas Current branches at the Confluence: one branch veers offshore while the inner part subducts and flows north along the slope. At the Confluence, the Subantarctic and Subtropical Front show large synoptic (800 km) and interannual migrations (300 km) compared to rather small seasonal changes (<150 km).

1. Introduction

The Malvinas Current (MC) is a cold and nutrient-rich current that originates in Drake Passage, where the steep topography forces the northernmost branch of the Antarctic Circumpolar Current (ACC), the Subantarctic Front (SAF), to turn northward and enter the western Argentine Basin. The MC, which follows the SAF (Figure 1a), is an intense current flowing northward along the Patagonian shelf break along the 1,000–2,000 m isobaths. The MC carries fresh Subantarctic waters that enrich the Patagonian shelf with nutrients and sustain the high productivity of this region (Acha et al., 2004; Carranza et al., 2017; Romero et al., 2006; Valla and Piola, 2015). At 38°S, the MC encounters the warm-salty poleward flowing Brazil Current (BC) which follows the Subtropical Front (STF, Figure 1a). This region is known as the Brazil-Malvinas Confluence (BMC). After the collision, both currents separate from the continental slope and veer offshore. A fraction of the BC follows the Brazil Current Front (BCF) that originates near the Confluence and flows northward as the eastern limb of a recirculation cell feeding back into the BC, while the other part of the BC follows the Subtropical Front and overshoots southward to about 45°S (known as BC overshoot) before bending back to the north (Figure 1a). The MC retroflects cyclonically toward the south, flowing side by side with the Brazil Current (BC) overshoot. The BMC (the region between the SAF and STF) is characterized by intense near surface velocities associated with fronts, eddies, meanders and filaments. The surface eddy kinetic energy (EKE) is among the greatest in the world ocean, with values exceeding 2000 cm^2s^{-2} (Figure 1b). In contrast, the EKE is rather modest upstream of the collision with values less than 600 cm^2s^{-2} for the BC and even smaller for the MC (< 200 cm^2s^{-2}, Artana et al., 2016).

The BC leaves the continental slope at about 38°S, that is nearly 15° north of the zero isoline in the mean wind stress curl (Figure 1 e). The role of the dynamics of two colliding jets has been invoked to explain the BC mean separation latitude (or mean STF location) with

114 theoretical and numerical models (e.g. Agra and Nof, 1993; Matano, 1993). Those studies
115 suggest that the MC imparts a momentum certainly responsible for determining the mean
116 latitude of separation of the BC from the slope. The latitude of separation of the STF from the
117 slope has been observed to vary at different time scales. At the seasonal scale the location of
118 the separation of the STF from the slope shows excursion of about 200 km along the 2,000 m
119 isobath with a poleward migration in austral summer and equatorward shift in winter (Saraceno
120 et al., 2005). At longer time scales, Lumpkin and Garzoli (2011) observed a southern shift of
121 the latitude of the STF from October 1992 to December 2007 of about 0.6 to 0.9° per decade
122 and suggested that this trend was part of a longer-term oscillation.
123 *In situ* time series near the BMC are rather scarce. Current meter mooring data in the MC have
124 been obtained at approximately 41°S along Jason2 track #26 (Figure 1d) near the Confluence
125 with the BC at three different times: in 1993–1995 (Vivier and Provost, 1999a), 2001–2003
126 (Spadone and Provost, 2009), and 2014–2015 (Paniagua et al., 2018). At 41°S, the MC has
127 mainly a barotropic equivalent structure due to the weak stratification and the steep topography
128 (Vivier and Provost, 1999a), and is made of one single core in contrast to the several narrow
129 jets observed south of 42°S (Piola et al., 2013). Artana et al. (2018a) used a look-up table (LUT)
130 method to compute the MC transport time series at 41°S. Combining altimetric data and the *in*
131 *situ* data sets from the three 10 years apart mooring deployments a coherent and accurate
132 volume transport time series was obtained. The mean MC transport over 24 years (1993-2016)
133 in the upper 1,500 m was 37.1 Sv and the standard deviation 6.6 Sv. Artana et al. (2018a)
134 showed that transport extrema at 41°S are not driven by upstream conditions: maxima are
135 associated with cyclonic eddies that propagated from the south following the 4,000 m isobath,
136 while minima result from large anticyclonic anomalies shed by the Brazil Current overshoot.
137 Numerical studies of the region have been hampered by the difficulty to simulate the location
138 of the Confluence. Indeed, the location of the Confluence is highly sensitive to the bottom

139 friction representation and to the vertical and horizontal resolutions of the model (Combes and
140 Matano, 2014). High-resolution ocean models that assimilate different types of observations
141 and in particular satellite altimetry (e.g. Lellouche et al., 2018) are a priori likely to have the
142 Confluence of the SAF and STF at the correct location.
143 Here we take advantage of the 25-year-long high-resolution (1/12°) global Mercator Ocean
144 physical reanalysis to revisit the BMC region. At any location, these daily outputs provide
145 continuous three-dimensional time series that integrate information from *in situ* and satellite
146 data and from the atmospheric forcing. This analysis builds upon previous works that assessed
147 the performance of the reanalysis in the MC system (e.g. Artana et al., 2018b and c). The main
148 purpose of this paper is to examine variations in the MC at 41°S, in the BC at 36°S at different
149 time scales from synoptic to interannual and explore concomitant variations in the Confluence
150 region. The work includes further model assessment in the BMC.
151 This paper is organized as follows: Section 2 presents model outputs and satellite data and
152 recalls previous assessments of the Mercator-Ocean system performance in the MC. The
153 vertical structures in hydrography and velocities of the MC at 41°S, of the BC at 36°S and of
154 their Confluence on a section following the 2,000 m isobath are examined in section 3. Section
155 4 concentrates on volume transports in the MC at 41°S and the BC at 36°S comparing the
156 reanalysis with observations. Variations in the SAF and STF positions at the Confluence are
157 examined in section 5. Section 6 summarizes and concludes.
158
159 **2. Model Outputs and data**
160 **2.1 Mercator Ocean Global Reanalysis: GLORYS12**
161 We use daily means of 25 years (1993–2017) of high-resolution (1/12°) global Mercator Ocean
162 reanalysis (hereafter, GLORYS12) from Copernicus Marine Environment Monitoring Service
163 (CMEMS, http://marine.copernicus.eu/). GLORYS12 is based on the current real-time global

high-resolution forecasting CMEMS system PSY4V3 (Lellouche et al., 2018). Compared to PSY4V3, GLORYS12 reanalysis uses the reprocessed atmospheric forcing coming from the global atmospheric reanalysis ERA-Interim and benefits from a few changes in the system settings about observation errors. The model has 50 vertical levels with 22 levels in the upper 100 m leading to a vertical resolution of 1 m in the upper levels and 450 m near the bottom. The physical component of the model is the Nucleus for European Modeling of the Ocean platform (NEMO). The model assimilates observations using a reduced-order Kalman filter with a 3-D multivariate modal decomposition of the background error and a 7-day assimilation cycle (Lellouche et al., 2013). Along-track satellite altimetric data from CMEMS (Pujol et al., 2016), satellite Sea Surface Temperature from NOAA, Sea-Ice Concentration, and *in situ* temperature and salinity vertical profiles from the latest CORA *in situ* databases (Cabanes et al., 2013; Szekely et al., 2016) are jointly assimilated. A 3D-VAR scheme provides a 3-D correction for the slowly evolving large-scale biases in temperature and salinity when enough observations are available (Lellouche et al., 2018).

In a previous work, Artana et al. (2018b) evaluated the performance of the current real-time global forecasting system PSY4V3 in the Southwestern Atlantic Ocean. Ten years (2007–2016) of model outputs were compared to assimilated satellite and Argo float data and to independent *in situ* data that were not assimilated. The comparison showed that the PSY4V3 system correctly reproduces the general circulation and the complex hydrographic features of the Southwestern Atlantic Ocean. We found and excellent agreement between model sea surface height (SSH) and satellite SSH. The positions of the Subantarctic and Subtropical Fronts were defined with model SSH contours of 5 cm and 40 cm which correspond to the maxima in SSH gradient. Front detection criteria in potential density at 541 m were also established: the SAF and STF were associated with the 27.16 kg/m^3 and 26.95 kg/m^3 isocontours. The location of

188 the fronts inferred from potential density at 541 m was in good agreement with the location
189 inferred from SSH.
190 In a subsequent work we found a general agreement between GLORYS12 and PSY4V3, and
191 comparisons with observations showed that GLORYS12 is closer to the data than PSY4V3 in
192 the region of interest (Artana et al., 2018c).
193 **2.2 Satellite data:**
194 We used DUACS delayed time altimeter gridded product (Pujol et al., 2016) from CMEMS.
195 The "Updated" product includes data from all available altimeters at any given time. This
196 product has a spatial resolution of ¼° on a Mercator regular grid and a daily sampling. The
197 multi-satellite gridded product is based on a space-time interpolation and its actual temporal
198 resolution is 20 days (Pujol et al., 2018). Surface geostrophic velocities anomalies derived from
199 the Sea Level Anomaly (SLA) product were used to compute the Look Up Table transport time
200 series. The current SLA is computed relative to the global ¼° CNES-CLS13 Mean Dynamic
201 Topography (MDT), which is the mean of the sea surface height above the geoid over the period
202 1993-2012 (Rio et al., 2014). The CNES-CLS13 MDT was obtained from a combination of
203 space gravity measurements (from the GOCE and GRACE missions), altimetry satellite data
204 and *in situ* observations (temperature and salinity profiles from Argo floats, CTD, XBT casts
205 and surface velocities derived from the trajectory of drifting buoys). For this study, we also had
206 access to a beta version of the new CNES-CLS MDT (CNES-CLS18) calculated over the 1993-
207 2012 reference period on a 1/8° resolution grid (Rio et al., The new CNES-CLS18 Mean
208 Dynamic Topography solution, in preparation). Compared to the previous CNES-CLS13 MDT,
209 this new solution was calculated using the latest CNES-CLS15 altimetric Mean Sea Surface
210 (Pujol et al, 2018), the latest GOCE geoid model, GOCO05s (Fecher et al., 2017), as well as an
211 extended dataset of in-situ observations (SVP type drifting buoys and Argo floats covering the
212 period 1993-2016).

2.3 Wind forcing:

We used daily averages of the ERA-Interim winds interpolated onto the NEMO grid. The mean wind stress curl field is mostly positive between 15°S and 45°S with a zero isoline extending zonally across the Atlantic Basin between the 45°-50°S (Figure 1e). In the Southwest Atlantic, the STF, which marks the southern limit of the Brazil Current, is found 15° to the north of the wind stress curl zero isoline. The mean position of the wind stress curl maximum (between the 40-30°S latitude band) roughly corresponds to the position of the zero isoline of the zonal wind stress (τ_x =0, thick black line in Figure 1f) that is the limit between easterlies to the north and westerlies to the south. The position of the zero isoline in τ_x exhibits a seasonal cycle with a mean northern position in winter (blue isoline, Figure 1f) and a southward position in summer (red isoline in Figure 1f). The seasonal migration of the zero isoline of τ_x is large along South America (~ 1500 km at 55°W). We found that the intersection of the zero-line of the τ_x with a section following the 2,000 m isobath (magenta line in Figure 1f) was a useful proxy to monitoring wind variations near the Brazil-Malvinas Confluence.

3. Vertical structure of the MC and BC at the Brazil-Malvinas Confluence

We examined the vertical structure of the model velocities, temperature, salinity and density along three sections: one across the Malvinas Current at 41°S, one across the Brazil Current at 36°S and one across the Confluence along a section approximately following the 2,000 m isobath (Figure 1c and d). The MC section corresponds to part of Jason2 altimetric satellite track #26 (section at 41°S in Figure 1c and d) where three 10-years apart moorings (1993-1995, 2001-2003, 2014-2015 green, black and red diamonds in Figure 1d) were lined up. The BC section (section at 36°S in Figure 1c and d) was chosen perpendicular to the slope. The 2,000 m isobath was chosen because it falls close to the midpoint of the continental slope, it is rather straight and the MC and BC cores roughly lie above that depth. The 2,000m isobath section is

900-km long (extending from 42°S to 35.5°S) and crosses the MC and BC sections at km 200 and 870. Model velocities were decomposed into the along and across-slope components, i.e. parallel (V//) and perpendicular ($V^{\perp}$) to the local bottom slope. The statistics were computed using the 25 years of GLORYS12 with a daily resolution after removing the trends which are discussed in section 5.4.

3.1 Mean vertical structure in hydrography and velocity

At 41°S the modelled mean MC shows a velocity core with values larger than 40 cm/s extending down to 600 m depth (Figure 2, Ia). As expected, model mean SAF location (thick black line at km 40 in Figure 2.I corresponding to SSH= 5 cm and $\sigma_\theta = 27.16$ kg/m^3 at 541 m) coincides with the maximum of the surface velocity. The mean cross-slope velocity component is small (< 5 cm/s) and changes sign near the center of the MC core (Figure 2, Ib). Mean vertical velocities show positive values (>20 m/day) on the slope indicating a mean upwelling between 300 m and 1000 m depth (Figure 2 Ic). The modelled water mass structure is in remarkable agreement with the literature (e.g., Maamaatuaiahutapu et al., 1994). At 41°S, two distinct water masses can be identified between the surface and 1000 m (Figure 2 Id, Ie, If). The first 400 m of the water column are occupied with Subantarctic Surface Water (SASW, σ_θ<27.00 kg/m^3). The low salinities close to the surface to the west of the section correspond to a mixture of SASW with diluted shelf waters. Depths between ~ 600 m and 1000 m correspond to the Antarctic Intermediate Water (AAIW) with salinities less than 34.3 psu and temperature less than 4°C (27.00 <σ_θ<27.35 kg/m^3).

The mean BC at 36°S is shallower and weaker than the MC at 41°S: mean along-slope velocities larger than 30 cm/s are only found above 400 m. The maximum mean velocity does not exceed 40 cm/s and coincides with the mean STF position (red thick line in Figure 2 IIIa). Mean positive along-slope velocities are observed between 600 m and 1000 m depth (km 20-60) in opposite direction to the general southward mean BC flow. They are small (~ 5 cm/s) and

263 associated with relatively low temperatures (<5 °C) and salinities (<34.3 psu) (Figure 2 IIId
264 and IIIe), suggesting a contribution from the MC. We call this circulation feature MC
265 subsurface northward branch (it is further examined in section 3.4). Mean cross-slope velocities
266 at 36°S are small (<10 cm/s) with an offshore direction in the upper 600 m (Figure 2 IIIb). The
267 mean vertical velocities are positive (~ 10 m/day) on the slope between km 20 and 60 between
268 200 m and 1000 m depth (Figure 2 IIIc). The model water mass distribution at 36°S is in good
269 agreement with the description from Valla et al. (2018) and Maamaatuiahutapu et al. (1994).
270 The upper 200 m of the water column consist in warm (~ 20°C) and salty (>36 psu) Tropical
271 Waters (TW). The low salinities on the west part of the section correspond to TW diluted with
272 water from the shelf. The South Atlantic Central Water (SACW) with 5< θ <10 °C, 34.3< S
273 <35.7 psu is found between 200 and 600 m. The layer between 600 and 1000 m corresponds to
274 AAIW (34.3< S <34.4 psu and 3< θ <5 °C) (Figure 2 IIId, IIIe).
275 The section following the 2,000 m isobath illustrates the contrasts between the deep reaching
276 MC velocity core (30 cm/s extending down to 700m) and the shallower BC velocity core (30
277 cm/s above 200 m) (Figure 2 II a). The SAF (SSH = 5 cm and σ_θ = 27.16 kg/m^3 at 541m) mean
278 location is at km 400 and the STF (SSH= 40 cm and σ_θ = 26. 95 kg/m^3 at 541m) at km 700.
279 The mean positive across-slope velocities (larger than 15 cm/s) between the mean SAF and
280 STF position (400 - 700 km) correspond to the BC and MC veering offshore at their Confluence
281 (Figure IIb). The mean model properties illustrate how high-density waters carried by the MC
282 (σ > 26.9 kg/m^3) are subducted below the lighter BC waters as they flow northward (Figure 2
283 IId, IIe, IIf). Mean negative vertical velocities reaching 10 m/day at 800 m between km 300 and
284 500 are associated with MC water subduction (Figure 2IIc). Mean isopycnals are sharply tilted
285 in the Confluence region (Figure 2 II f).

286 **3.2 Vertical structure of standard deviations in hydrography and velocity**

The standard deviations (stds) of the model properties in the MC section are small below 100 m (V// std <10 cm/s, V⊥ std < 10 cm/s, w std <10 m/day, θ std < 0.3 °C, S std < 0.06 psu and σ_θ std < 0.06 kg/m^3, Figure 3 Ia-If). The MC is a rather steady current (surface EKE over the MC at 41°S is less than 200 cm^2/s^2, Figure 1b). The MC velocity stds are homogenous in the vertical reflecting the MC barotropic equivalent structure (Vivier and Provost 1999a and 1999b). The larger velocity stds in the outer part of the MC section (between km 100 and 140) are due to meanders and mesoscale eddies from the BC overshoot (Figure 3 Ia-f).

In contrast to the MC, the BC has a baroclinic structure and shows surface EKE in excess of 1,000 cm^2/s^2 at 36°S (Figure 1b). The standard deviations of the model properties in the BC section are large (V// std >25 cm/s, V⊥ std > 20 cm/s, w std > 10 m/day, θ std > 1°C, S std > 0.2 psu and σ_θ std > 0.1 kg/m^3) (Figure 3, IIIa-f). The relatively small std of the water properties close to the bottom at the location of the MC northward branch observed in the mean (Figure 2 III a), suggest that the MC subsurface northward branch is a quasi-permanent feature. The MC subsurface northward branch is further discussed in section 3.4.

The section along the 2,000 m isobath shows that the frontal region (between the SAF and STF km 400 and 700) hosts the largest stds for all model properties (θ std > 0.3 °C, S std > 0.09 psu , σ_θ std >0.09 kg/m^3, V// std and V⊥ std >15 cm/s and w std > 20 m/day down to 1000 m, Figure 3 IIa-IIf) with values well above those found in the BC and MC sections.

3.3 Seasonal cycle

As the amplitude and phase of the seasonal cycle vary from year to year, the seasonal cycle was estimated using a band-pass filter. A band-pass filter with a window of 140-400 days led to the stds shown in Figure 4 (with same scale as Figure 3 for sake of comparison). The amplitude of the seasonal cycle can be roughly estimated by multiplying the stds by a factor of √2. The amplitude of the resulting signal was not sensitive to the filter window.

311 The seasonal cycle contributes to a significant fraction of the stds shown in Figure 3. As
312 expected, in the upper 100 m, the seasonal cycle in potential temperature (std larger than 3°C
313 in the BC and 0.9°C in the MC) and density (std larger than 0.3 kg/m^3 in the BC and 0.2 kg/m^3
314 in the MC) amounts to more than 60 % of the total stds (Figure 4 I and III d-f and Figure 3).
315 Salinity variations due to the seasonal cycle account for about 40% of the total std (shown in
316 Figure 3 I and III e) in the upper 100 m and 30% below in the MC and in the BC. For the other
317 model variables, the seasonal cycle is responsible for about 40% of the std at all depths (Figure
318 4 a-c). Std values associated with the seasonal cycle are particularly large at the BMC (between
319 km 400 and 700) and extend down to 600 m ($V// > 10$ cm/s, $V\perp > 5$ cm/s, $\theta > 0.6$ °C $S > 0.03$ psu
320 and $\sigma > 0.03$ kg/m^3) (Figure 4 II a-f).
321 To describe the seasonal cycle further, we performed an EOF analysis of the joint velocity and
322 density ($V//$, $V\perp$ and σ) fields along the 2,000 m isobath. The first EOF explains 30% of the
323 total variance (shown in Figure 3 II). The time series (Figure 5a) features dominant energy
324 peaks at the semi-annual and annual periods and much less significant energy at the 50-70 days
325 band period. The positive phase (related to the austral summer) corresponds to a strengthening
326 of the BC and a 150 km-southward migration of the STF position (deduced from the potential
327 density criteria at 541 m cf section 2.1). In contrast, the MC strength and SAF position do not
328 change much compared to the mean (Figure 5c and 5d). In summer, the distance between the
329 SAF and STF reduces to less than 100 km and the isopycnal slopes between the fronts steepen
330 (Figure 5d). The negative phase (related to the austral winter) expresses a weakening of the BC
331 with the STF located 100 km to the north of its mean position (Figure 5e to be compared with
332 Figure 5 c) and little change in the MC velocities and SAF location. The distance between the
333 SAF and the STF increases to 400 km.
334 In summary, the MC appears as a strong steady current compared to the weaker and highly
335 variable BC. The seasonal cycle in the Confluence region comprises migrations of the STF

position (150 km) and changes in the BC strength (more than 20 cm/s in the core) while the MC strength and the SAF position remain mostly unchanged. The seasonal cycle at the confluence is further examined in section 5.

3.4 Synoptic scale

The snapshot from Figure 6 further illustrates the model performances at the BMC. Salinity maps at different depths (Figure 6 a, b, c) show the BC leaving the coast at 39°S (150 km to the south of its mean position), the MC branching at 40°S (an inner branch keeping flowing north and an outer branch retroflecting to the south) and a rich mesoscale field with a large (100 km diameter) salty anticyclonic eddy centered at 54°W and 42°S and smaller structures such as the 25 km diameter eddy at 57°W 45°S tied to the large anticyclonic eddy with a 100 km-long filament (Figure 6 b). Similar mesoscale structures have been documented in the Confluence region from high resolution (1 km) satellite imagery (Barré et al., 2006). Fresh water (S <32 psu) from the Rio de la Plata is exported offshore through the Confluence between the SAF and the STF (Figure 6 a) as noted in hydrographic observations (Provost et al., 1995) and satellite data (Guerrero et al., 2014).

The MC core velocities at 41°S are slightly below their mean values while the strong core at is 20 cm/s larger than the mean above 300 m (Figure 6 Id and IIId). The BC waters lighter than 26.9 kg/m^3 extend down to 500 m (Figure 6 IIIf). Sharply tilted isopycnals at the confluence correspond to the MC branch subducting below the BC (between km 400 and 500) (Figure 6 IIf). Associated synoptic vertical velocities are negative and on the order of 100 m/day (Figure 6 IIg). After subducting, the MC branch keeps flowing north pushing the BC to upper levels and positive vertical velocities are observed (>50 m/day) between km 500 and 600 (Figure 6 IIg). Positive along-slope velocities (>10 cm/s) associated with the northward MC branch, are observed in the confluence section at km 600 (Figure 6 IId) and at 36°S along the slope below 300 m depth (Figure 6 IIId). This branch of the MC is seen in the salinity map at 500 m up to

361 36°S along the slope (Figure 6 c). The branching of the MC in the model is consistent with
362 hydrographic observations (e.g. Provost et al., 1995) which showed that the eastern branch of
363 the MC returned south, while the western one squeezed along the continental slope and sank
364 below the BC, managing to propagate as far as 36.3°S. To further document the MC subsurface
365 northward branch along the slope we show time series of the V//, T and S (Figure 7) at 763 m
366 depth at km 40 of the 36°S BC section (positive black dot in Figure 6 III a). Positive along slope
367 velocities associated with the MC subsurface branch can reach values as large as 50 cm/s
368 (Figure 7a). The year 2006 stands out with large (>40 cm/s) northward velocities over 4 months.
369 The positive along slope velocities are accompanied with a decrease of temperature (<3 °C)
370 and salinity (34.1 psu) associated with MC (Figure 7). The time series feature significant energy
371 peaks at the 50-110 days period band (possibly associated with coastal trapped waves; e.g.,
372 Lebedev and Nof 1996; Vivier et al., 2001) and much less energy at the annual and semiannual
373 periods. The salinity and temperature time series present a low-frequency modulation with low
374 salinity and temperature values during the period 1997-2003 and larger ones during the prior
375 and later years (Figure 7b). This low frequency-modulation is reminiscent of the salinity
376 minimum observed in the MC recirculation during the period 1997-2003 (Artana et al., 2018c).
377 We now examine the model skills in reproducing the MC and BC volume transports near the
378 Confluence.
379
380 **4. Volume transports of the MC and BC near the Confluence**
381 **4.1 Volume transport time series of the MC at 41°S**
382 The MC volume transport over the upper 1,500 m of the water column across the 41°S section
383 (Figure 1 c) was reconstructed over 25 years (1993-2017) from *in situ* and satellite altimetry
384 data using the Look Up Table (LUT) method (Artana et al., 2018a). The LUT was built with
385 the 10 years apart current meter data (1993-1995 green, 2001-2003 black and 2014-2015 red

386 diamonds in Figure 1d). A mean cross-track surface velocity was adjusted at each mooring
387 location using an iterative error/correction scheme with the CNES-CLS13 mean surface
388 geostrophic velocities as a first guess (Artana et al., 2018a). The new CNES-CLS-18 MDT
389 provides mean surface geostrophic velocities larger than those derived from CNES-CLS13 and
390 consistent to those from the (independent) LUT method, with a maximum of 57 cm/s at km 50
391 (Figure 8a). The 25 year-long LUT transport time series has a mean of 37 Sv and a standard
392 deviation of 6.7 Sv (Figure 8b) and does not present any significant trend. The yearly averages
393 of the volume transport suggest a low-frequency modulation with a time scale of several years
394 (Figure 8c).
395 Model velocities were used to compute volume transport time series considering several depths
396 of integration (1,500 m, 1,000 m and 900 m). The mean model transport from the surface to
397 1,500 m is 10 Sv larger than the LUT mean transport as model velocities are larger than
398 observations at depths on the outer slope (see Figure 5 in Artana et al., 2018b). The best
399 agreement with the LUT transport was found for an integration depth of 900 m with a difference
400 less than 1 Sv for the mean, 0.7 Sv for the std and a correlation coefficient of 0.75 (Figure 8b).
401 The model transport time series does not present any significant trend and reproduces the
402 observed interannual variations (the largest difference is only 3 Sv in 1996, Figure 8c).
403 Variance preserving spectra of the two transport time series show significant salient peaks at
404 similar periods (intraseasonal, semi-annual and annual period, Figure 8d). The spectrum of the
405 model transport time series presents larger energy between periods 50 and 100 days than the
406 LUT transport spectrum. This period band has been associated with baroclinic coastal trapped
407 waves propagating along the continental slope (Vivier et al., 2001). The differences around
408 these frequencies suggest that coastal trapped waves may be better resolved in the model than
409 in the gridded altimetry product used in the LUT method. The spectral content of the model
410 transport time series shows a similar modulation to that of the LUT transport time series (Figure

411 8e and Artana et al., 2018a) with a more energetic annual component during the years 2001-
412 2007.

413 **4.2 Volume transport of the BC**

414 Model outputs were used to compute the BC transport across two sections located at 37°S and
415 36°S. Sensitivity to the depth of integration was carefully examined. The BC transport time
416 series were computed integrating the along-slope negative velocities from the surface to 1,500
417 m, 1,000 m, 900 m and 800 m. The different vertical integration limits yielded highly correlated
418 transport times series (r = 0.99) and small changes in the mean (5 Sv) and std (3 Sv). The BC
419 transport time series integrated down to 900 m (like model MC transport) presents a lower mean
420 (23.0 Sv at 36°S and 26.7 Sv at 37°S) and a larger standard deviation (11.0 and 15.0 Sv
421 respectively) than the MC transport time series (mean: 38.0 Sv and std: 7.4 Sv). Considering
422 that the mean BC transport increases with latitude (Garzoli et al., 2013), the order of magnitude
423 provided by the reanalysis at 36 and 37°S is consistent with previous estimates of the mean BC
424 transport derived from satellite altimetry and Argo data (22.2 Sv at 36°S in the upper 2,000 m
425 in Schmid, 2014), from inverted echo sounders (23.5 Sv at 35.2°S in the upper 1000 m in
426 Garzoli 1993) and from XBT data and satellite altimetry (19.4 Sv at 35°S in the upper 800 m
427 from Garzoli et al., 2013). The standard deviation of the BC transport of 11 Sv for daily
428 resolution reduces to 6 Sv for monthly means in agreement with the time series at a monthly
429 resolution from Schmid (2014) and Garzoli et al. (2013).
430 The transport time series at 37°S and 36°S are correlated (r = 0.4, 99% confidence level) at lag
431 20 days. The 25-year-long linear trend for the two transport time series is 0.36 Sv/y significant
432 above the 90% confidence level. The transport time series at 36°S is shown in Figure 9a.
433 The BC transport time series at 36°S shows large interannual variations with a maximum of 30
434 Sv in 2014 and a minimum of 14 Sv in 1998 (Figure 9b). Salient energy peaks are found
435 between the 50- and 150-day periods and at the annual period (Figure 9c). Similar energy peaks

436 have been observed in inverted echo sounders deployed in the BC at 37°S (Garzoli and Bianchi,
437 1987). The spectral content is modulated over time (Figure 9d), in particular, energy at the
438 annual period is large from 2001 to 2012. A wavelet coherence analysis of the MC transport
439 time series at 41°S and the BC transport time series at 36°S indicates that the MC and the BC
440 are not correlated at any periodicity (not shown).
441
442 **5. SAF and STF location near the Confluence**
443 Mercator Ocean reanalysis provides correct mean locations for the SAF and STF at the
444 Confluence and a value of 38.0 Sv for the mean MC volume transport at 41°S in agreement
445 with the LUT and a value of 23.0 Sv (26.7 Sv) for the mean BC transport at 36°S (37°S) in
446 agreement with the existing literature. These results are consistent with a strong steady
447 Malvinas Current forcing the mean separation latitude of a weaker BC at 15° north of the zero
448 of the mean wind stress curl as suggested in Agra and Nof (1993) or in Matano (1993).
449 We examined variations of the SAF and STF locations at different time scales and their relation
450 with current transport and wind forcing. Monitoring the temporal evolution of the fronts
451 position at the synoptic scale is quite challenging due to the energetic mesoscale field (section
452 5.1). We investigated the seasonal (section 5.2) and interannual (section 5.3) variations of the
453 SAF and STF positions at the confluence in relation with the latitude of the zero isoline of the
454 τ_x across a section following the 2,000 m isobath between 26°S and 38°S (magenta section in
455 Figure 1 f, hereafter we called this position τ_x=0). Finally, we examined long term variations in
456 SAF and STF positions and in the model properties at the confluence location (section 5.4).
457 **5.1 Synoptic scale**
458 The SAF (white isoline in Figure 10a) and STF (purple isoline in Figure 10a) positions above
459 the 2,000 m isobath vary over a wide range of spatial (about 800 km) and temporal (synoptic
460 to interannual) scales. The distance between the SAF and STF above the 2,000 m isobath ranges

461 from almost zero when the fronts are merged into a narrow front (e.g. beginning of 2017) to
462 over 800 km when the BMC region is filled with meanders and eddies (e.g. end of 2001) (Figure
463 10a). The SAF and STF isolines are frequently tortuous as the fronts meander and shed eddies,
464 impeding the construction of time series of the fronts position with a daily resolution as
465 evidenced in the close up on the last period of mooring observations (January 2015- December
466 2015, Figure 10b). This year has been carefully examined (Ferrari et al., 2017; Artana et al.,
467 2018a; Paniagua et al., 2018; Orue-Echevarria et al., 2019). From January 2015 to October
468 2015, the SAF and STF were located to the south of their mean position while the MC transport
469 at 41°S was below its mean and the BC transports at 37°S and 36°S were highly variable (Figure
470 10c). The fronts moved northward from September to October while the MC transport increased
471 and the BC transport was close to its mean. From October to December, the fronts were located
472 to the north of their mean position and the MC and BC transports at 41°S and 36°S (north of
473 the front position) were above their mean.
474 Interestingly, the wind stress curl interpolated over the 2,000 m isobath shows a sharp local
475 minimum (negative values) coinciding with the front position (Figure 10d). The mean wind
476 stress curl also presents a local minimum at 55°W and 38°S at the mean location of the
477 Confluence (Figure 1f). This feature at the Confluence suggests a local atmospheric response
478 due to a thermal or current feedback as sea surface temperature anomalies or ocean current
479 anomalies can alter wind patterns (e.g., Chelton et al., 2007).

480 **5.2 Seasonal cycle**

481 The seasonal position of the STF and SAF defined with isolines (respectively 40 and 5 cm) of
482 monthly mean model SSH over the 25 years of the reanalysis are shown in Figure 11a. The
483 fronts move northward during austral winter and southward during summer (Figure 11 a). The
484 STF pivots at a fixed point located at 53°S and 40°S in agreement with Saraceno et al. (2005).
485 The seasonal displacements are small: 150 km (1.5° in latitude) for the STF and 50 km for the

SAF along the 2,000 m isobath (Figure 11 a and c). As a consequence, the distance between the SAF and STF along the 2,000 m isobath is larger during winter (~ 400 km) than during summer (~200 km, Figure 11 b). This is consistent with the EOF analysis of section 3.3 (Figure 5). In contrast, the seasonal migration of the zero isoline of the zonal wind stress is large (1,500 km – section 2.3). At the seasonal scale, the STF position, the BC transports (at 36 or 37°S) covary with τ_x=0 with a lag of about 2 months (Figure 11 c and d). The τ_x=0 reaches its southernmost position of 27.50°S in June while the BC transport is minimum in July-August and the STF latitude minimum (36.30°S) occurs 2 months later in August. However, covariances do not imply causality, cause and effect cannot be disentangled.

5.3 Interannual and long-term variations:

The annual mean STF and SAF positions on the 2,000 m isobath vary over a latitudinal range larger than 3° for the STF and 1.5° for the SAF (Figure 12a b and d). The STF and SAF are in their northward most position in the early 1990s (around 36.5°S and 39°S respectively). During the 2000-2010 decade the annual mean STF and SAF are in a southern location around 37°S and 39.5°S respectively. The last decade shows large interannual variations: indeed, while the mean positions of the SAF and STF are relatively south in 2015 (40.5°S and 38°S), they are back north like in the 1990s in 2016. In 2017, the SAF and STF mean position are back south (40.3°S and 39.5°S). The annual mean distance between the STF and SAF above the 2,000 m isobath (Figure 10 c) ranges from 150 km (in 2017) to 450 km (in 1994). Large interannual variations in the STF and in the τ_x=0 location occur from 2000 to 2017 (Figure 12 e). In particular, years 1998, 2004, 2011, 2015 and 2017 correspond to southernmost positions of the STF and τ_x=0 isoline. The southernmost position of the STF in 2017 is congruent with a southward position of τ_x=0, a strong BC transport at 36°S and a weak MC transport at 41°S. The SAF remains at a rather stable position during the years of large interannual variations in the position of the τ_x=0 (from 2000-2010) and seems to covary with the MC transport at 41°S.

511 Again, causality relations between front positions, current transports and wind forcing are not
512 established.
513 The time series of the STF position suggests a southward migration of the front from 1993 to
514 2006 in agreement with Goni et al. (2011) and Lumpkin and Garzoli (2011). During the
515 following years the front position is highly variable. Long-term variations in the SAF and STF
516 position and in the vertical structure model properties at the confluence region are further
517 examined below.

518 **5.4 Twenty-five-year trends**

519 We tentatively examined linear trends in water properties in the 25-year reanalysis: they are
520 significant above the 99% confidence level (Figure 13 a, b, c, d, e). The changes in the SAF
521 and STF positions associated with the density trend were computed after adding the trend
522 (Figure 13e) to the mean field (Figure 2f) using the criteria in potential density at 541 m (Figure
523 13f) (cf section 2.1).
524 Trends are large in the BC which becomes more intense (~12.5 cm/s over the 25 years), warmer
525 (~2.5°C) and saltier (0.375 psu) in the first 1000 m at 36°S (Figure 13 III a d e). The BC
526 becomes denser in the first 200 m due an increase in salinity and lighter below due to the
527 warming trend (Figure 13 III e). Trends in the MC are small (Figure 13 I) with weaker along-
528 slope velocities (< 0.1 cm/year) in the inner MC (Figure 13 I a) and a lightening of 0.002
529 kg/m^3/year in the upper 100 m (Figure 13 I d and e).
530 The trends in the northern part (km 400 -1000) of the along 2,000m isobath section reflect a
531 southward displacement of the confluence region with an intensified southward flow (Figure
532 13 IIa) with warmer, saltier and lighter waters (Figure 13 II c, d, e). The increase in the across-
533 slope velocities between km 200 and 600 (at a rate of 0.2 cm/y) (Figure 13 II b) is congruent
534 with the southward displacement of the confluence and a larger offshore water export. Indeed,
535 trends in the density field lead to an estimation of a southern displacement of 50 km for the

SAF and 150 km for the STF (Figure 13 f). As a consequence, the mean distance between the SAF and STF over the 2,000 m isobath reduced from 300 to 200 km.

6 Summary and discussion

This analysis of the upper 1000 m in the BMC region builds upon previous works that assessed the performance of Mercator-Ocean high-resolution (1/12°) ocean reanalysis GLORYS12 in the MC. The BMC is a complex region in terms of water mass structure (e.g. Maamaatuaiahutapu et al., 1992, 1994; Valla et al., 2018) and circulation (Provost et al., 1995; Orue-Echevarria et al., 2019). The model is consistent with present knowledge of the BMC and provides further insights on variations from synoptic to interannual time scales in the region. The model reproduces the contrast between the highly variable and baroclinic BC and the rather stable and more barotropic MC variations. Daily transport time series of the MC and BC across the 41°S, 36°S and 37°S sections were computed considering a depth of integration of 900 m. The MC transport derived from model outputs (mean of 37Sv and std of 6 Sv) has a similar mean than the LUT transport derived from observations and satellite altimetry (Artana et la., 2018 a) and are highly correlated (0.75). The daily BC transport time series at 37°S (36°S) with a mean of 26.7 Sv (23.0 Sv) and a std of 15.0 Sv (11.0 Sv) is consistent with estimates derived from satellite altimetry and Argo data (22.2 Sv at 36°S in the upper 2,000 m in Schmid, 2014) and from XBT data and satellite altimetry (19.4 Sv at 35°S in the upper 800 m from Garzoli et al., 2013). The model mean MC transport exceeds the mean BC transport by at least 12 Sv and possibly forces the BC to separate from the coast 15°S north of the wind stress zero as suggested in numerical and theoretical models (Agra and Nof, 1993; Matano, 1993).

A synoptic situation during the last MC mooring period, a year we carefully studied (Ferrari et al., 2017; Artana et al., 2018a; Paniagua et al., 2018) illustrates the model performance in this region. The model reproduces the rich mesoscale activity from the Confluence region showing

561 filaments and small eddies as those observed in high resolution satellite imagery (Barré et al.,
562 2006). The export of the Rio de La Plata water far away from the coast between the SAF and
563 STF documented in hydrographic observations (Provost et al., 1995) and satellite data
564 (Guerrero et al., 2014) is well represented in the model. The model shows the branching of the
565 MC near the Confluence (e.g., Provost et al., 1995), with an outer branch returning south and
566 an inner one sinking below the BC and flowing northward along the continental slope reaching
567 36°S. The along-slope velocity at 36°S below 600 m close to the slope (mean of + 4 cm/s)
568 shows recurrent positive peaks above 40 cm/s at periods between 50 and 110 days that can be
569 associated with Kelvin waves propagating along the slope (Lebedev and Nof, 1996; Vivier et
570 al., 2001). The water properties of the MC northward subsurface branch show a long-term
571 modulation with a salinity minimum in the period 1997-2003 reminiscent of the freshening
572 observed by Artana et al., (2018 c) in the MC recirculation region.
573 The SAF and STF positions above the 2,000 m isobath vary over a wide range of spatial (about
574 800 km) and temporal scales (synoptic to interannual). The region between the SAF and STF
575 is recurrently filled with mesoscale and eddies preventing the construction of a time series of
576 the front position with a daily resolution. The seasonal migrations of the SAF and STF positions
577 at the Confluence are small. The STF seasonal migrations of 150 km over the 2,000 m isobath
578 lag with seasonal variations of the BC transport (of 15 Sv with a 1-month lag) and with the
579 position of the zero isoline of τ_x (of 1500 km with a 2-month lag). At the seasonal time scale
580 the SAF and the MC transport remain mostly unchanged. The SAF and STF vary over a larger
581 range at the interannual scale (300 and 200 km respectively). The fronts were in their northern
582 position in the 90s (around 36.5°S for the STF and 39°S for the SAF) and moved southward
583 during the period 2000-2010 (SAF around 39.5°S and STF around 38.3°S). These southward
584 migrations of the fronts are in agreement with previous observational or modeling studies (e.g.,
585 Lumpkin and Garzoli, 2011; Goni, 2011; Combes and Matano, 2014). The next decade (2010-

2016) presents large year-to-year variations. The positions of the STF and the zero isoline of τ_x seem to covary. Overall, the cause of the observed changes in the SAF and STF position have yet to be established.

Linear trends in the 25-year-long reanalysis suggest an increase in the BC salinity of 0.37 psu and a warming of 2.5°C at 36°S. The BC salinity increase could be related with an intensification of the global water cycle (meaning and enhancement in the evaporation-precipitation water fluxes) (e.g., Durack et al., 2012). In particular, several studies have shown a long-term salinity increase in the tropical waters (in the evaporation-dominating latitudes) which are carried southward by the BC (e.g., Boyer et al., 2005; Durack et al., 2012). The positive temperature trend observed at 36°S is consistent with the fast warming observed in the subtropical western boundary currents at rate 2 to 3 times faster than the global rates (e.g., Wu et al., 2012, Yang et al., 2016). The positive salinity and temperature trends result in an increase of the BC stratification. The MC registered a surface freshening of 0.1 psu in agreement with the negative salinity trend observed in the waters north of the ACC (e.g., Böning et al., 2008, Naveira Garabato et al., 2009, Purich et al., 2018). The BC becomes more intense by 12.5 cm/years at 36°S while the MC velocity trends are small at 41°S. The model trends at the confluence suggest a southward migration of the SAF and STF of 50 and 150 km over 25 years.

Acknowledgments:

The authors are grateful to the CNES (Centre National d'Etudes Spatiales) for constant support. This study is a contribution to EUMETSAT/CNES DSP/OT/12-2118. We thank Nathalie Lefevre. Camila Artana acknowledges funding the European AtantOS project (grant agreement 633211). The satellite data and model outputs are available at Copernicus Marine Environment Monitoring Service (CMEMS; https://marine.copernicus.eu/).

611 References:

612 Acha, E. M., Mianzan, H. W., Guerrero, R. A., Favero, M., and Bava, J, (2004). Marine fronts
613 at the continental shelves of austral South America: physical and ecological processes.
614 *Journal of Marine Systems*, 44(1-2), 83-105, doi: 10.1016/j.jmarsys.2003.09.005

615 Agra, C. and Nof, D. (1993) Collision and separation of boundary currents. *Deep Sea Research*
616 I, 40, 2259-2282, doi:10.1016/0967-0637(93)90103-A

617 Artana C., R. Ferrari, Z. Koenig, M. Saraceno, A. Piola and C. Provost (2016). Malvinas
618 Current variability from Argo floats and satellite altimetry. *Journal of Geophysical*
619 *Research, Oceans*, doi:10.1002/2016JC011889.

620 Artana C., R. Ferrari, Z. Koenig, N. Sennéchael, M. Saraceno, A.R. Piola and C. Provost
621 (2018a). Malvinas Current volume transport at 41°S: a 24–year long time series
622 consistent with mooring data from 3 decades and satellite altimetry. *Journal of*
623 *Geophysical Research, Oceans*, doi :10.1002/2017JC013600.

624 Artana C., J.M. Lellouche, Y.H. Park, G. Garric, Z. Koenig, N. Sennéchael, R. Ferrari, A. Piola,
625 M. Saraceno and C. Provost (2018b). Fronts of the Malvinas Current System: surface and
626 subsurface expressions revealed by satellite altimetry, Argo floats, and Mercator
627 operational model outputs. *Journal of Geophysical Research, Oceans*, doi
628 :10.1029/2018JC013887.

629 Artana C., J.-M. Lellouche, N. Sennéchael and C. Provost (2018c). The open-ocean side of the
630 Malvinas Current in Argo float data and 25 years of reanalyses from Mercator operational
631 system. *Journal of Geophysical Research, Oceans*, 123, 8489–8507, doi:
632 10.1029/2018JC014528.

633 Barré N., C. Provost and M. Saraceno (2006). Spatial and temporal scales of the Brazil-
634 Malvinas Confluence documented by simultaneous MODIS Aqua 1.1-km resolution SST

635 and color images. *Journal of Advances in Space Research*, 37, 4, 770-786,
636 doi:10.1016/j.asr.2005.09.026.
637 Böning, C. W., A. Dispert, M. Visbeck, S.R. Rintoul and F.U Schwarzkopf (2008). The
638 response of the Antarctic Circumpolar Current to recent climate change. *Nature*
639 *Geoscience*, 1(12), 864–869, doi: 10.1038/ngeo362.
640 Boyer T. P., S. Levitus, J. I. Antonov, R. A. Locarnini, and H. E. Garcia (2005), Linear trends
641 in salinity for the World Ocean, 1955—1998, *Geophysical Research. Lett.,* 32, L01604,
642 doi:10.1029/2004GL021791.
643 Cabanes, C., A. Grouazel, K. V. Schuckmann, M. Hamon, V. Turpin, C. Coatanoan, ... & C.
644 D. Boyer Montégut (2013). The CORA dataset: validation and diagnostics of in-situ
645 ocean temperature and salinity measurements. *Ocean Science*, 9(1), 1-18, doi:
646 10.5194/os-9-1-2013
647 Carranza, M. M., S. T. Gille, A. R. Piola, M. Charo, and S. I. Romero (2017). Wind modulation
648 of upwelling at the shelf-break front off Patagonia: Observational evidence. *Journal of*
649 *Geophysical Research: Oceans*, 122(3), 2401-2421, doi: 10.1002/2016JC012059.
650 Chelton, D. B., M.G Schlax and R.M. Samelson (2007). Summertime coupling between sea
651 surface temperature and wind stress in the California Current System. Journal of Physical
652 Oceanography, 37(3), 495– 517, doi: /10.1175/JPO3025.1.
653 Combes, V., and R. P. Matano (2014). Trends in the Brazil/Malvinas Confluence region,
654 *Geophysical Research Letters*, 41, 8971–8977, doi:10.1002/2014GL062523.
655 Durack, P. J., S.E. Wijffels, and R.J. Matear (2012). Ocean salinities reveal strong global water
656 cycle intensification during 1950 to 2000. *science*, 336(6080), 455-458, doi:
657 10.1126/science.1212222.

Fecher, T., R. Pail, and T. Gruber (2017). GOCO05c: A new combined gravity field model based on full normal equations and regionally varying weighting. S*urveys in Geophysics*, 38(3), 571–590, doi: 10.1007/s10712-016-9406-y.

Ferrari R., C. Artana, M. Saraceno, A.R. Piola, and C. Provost (2017). Satellite altimetry and current–meter velocities inthe Malvinas Current at 41°S: comparisons and modes of variations. *Journal of Geophysical Research, Oceans*, doi: 10.1002/2017JC013340.

Garzoli, S.L and A. Bianchi (1987). Time-Space Variability of the Local Dynamics of the Malvinas-Brazil Confluence as revealed by Inverted Echo Sounders. *Journal of geophysical research, Oceans*, 92, C2, 1914-1922, doi: 10.1029/JC092iC02p01914.

Garzoli, S. L. (1993). Geostrophic velocity and transport variability in the Brazil-Malvinas Confluence. *Deep Sea Research Part I: Oceanographic Research Papers*, 40,7, 1379-1403, doi: 10.1016/0967-0637(93)90118-M.

Garzoli, S. L., M. O. Baringer, S. Dong, R. C. Perez & Q. Yao (2013). South Atlantic meridional fluxes. *Deep Sea Research Part I: Oceanographic Research Papers*, 71, 21-32, doi: 10.1016/j.dsr.2012.09.003.

Goni, G. J., F. Bringas, and P. N. DiNezio (2011). Observed low frequency variability of the Brazil Current front, *Journal of Geophysical Research, Oceans*, 116, C10037, doi:10.1029/2011JC007198.

Guerrero R.A., A.R. Piola, H. Fenco et al. (2014). The salinity signature of the cross-shelf exchanges in the southwestern Atlantic Ocean: satellite observations. *Journal of Geophysical Research, Oceans*, 119, doi: 10.1002/2014JC10113.

Lebedev, I., and D. Nof. (1996). The drifting confluence zone. *Journal of Physical Oceanography*, 26(11), 2429-2448, doi: 10.1175/1520-0485.

Lellouche, J.-M., Greiner, E., Le Galloudec, O., Garric, G., Regnier, C., Drevillon, M., et al. (2018). Recent updates on the Copernicus Marine Service global ocean monitoring and

683 forecasting real-time 1/12° high resolution system. *Ocean Science Discussions*, doi :
684 10.5194/os-2018-15.
685 Lellouche, J.-M., Le Galloudec, O., Drevillon, M., Regnier, C., Greiner, E., Garric, G., et al.
686 (2013). Evaluation of real time and future global monitoring and forecasting systems at
687 Mercator Ocean. *Ocean Science Discussions*, 9, 1123–1185.
688 Lumpkin, R., and S. L. Garzoli (2011). Interannual to decadal variability in the southwestern
689 Atlantic surface circulation, *Journal of Geophysiscal Research, Oceans*, 116, C01014,
690 doi:10.1029/2010JC006285.
691 Maamaatuaiahutapu K., V.C. Garçon, C. Provost, M. Boulahdid and A.P. Osiroff, (1992).
692 Brazil Malvinas Confluence: water mass composition. *Journal of Geophysical Research,*
693 *Oceans, 97(C6), 9493-950*. doi: 10.1029/92JC00484.
694 Maamaatuaiahutapu, K., V. Garçon, C. Provost, M. Boulahdid, and A. A. Bianchi, (1994).
695 Spring and winter water mass composition in the Brazil-Malvinas Confluence, *Journal of*
696 *Marine Research*, 52, 397-426.
697 Matano, R. P. (1993). On the separation of the Brazil Current from the coast. *Journal of Physical*
698 *Oceanography*, 23(1), 79-90.
699 Naveira Garabato, A. C., Jullion, L., Stevens, D. P., Heywood, K. J., and King, B. A, (2009).
700 Variability of subantarctic mode water and Antarctic Intermediate Water in the Drake
701 Passage during the late-twentieth and early-twenty-first centuries. *Journal of Climate*,
702 22(13), 3661– 3688. doi: 10.1175/2009JCLI2621.1
703 Orue-Echevarria D., J.L. Pelegri, F. Machin, Z. Hernandez-Guerra, & M. Emelianov (2019).
704 Inverse modeling the Brazil-Malvinas Confluence. *Journal of Geophysical Research,*
705 *Oceans*, 124, 527-554, doi:10.1029/2018JC014733.
706 Paniagua G., M. Saraceno, A. Piola, C. Provost, R. Guerrero, R. Ferrari, L. Lago, and C. Artana,
707 (2018). Dynamics of the Malvinas Current at 41ºS: First assessment of temperature and

salinity temporal variability. *Journal of Geophysical Research, Oceans*, doi:10.1029/2017JC013666.

Piola, A. R., B. C. Franco, E. D. Palma, and M. Saraceno (2013). Multiple jets in the Malvinas Current. *Journal of Geophysical Research, Oceans*, 118, 2107–2117, doi: 10.1002/jgrc.20170.

Provost C., S. Gana, V. Garçon, K. Maamaatuaiahutapu and M. England, (1995). Hydrographic conditions during austral summer 1990 in the Brazil/Malvinas Confluence region. *Journal of Geophysical Research, Oceans*, vol. 100, C6, 10655-10682, doi:10.1029/94JC02864.

Pujol, M-I, P. Scheffer, Y. Faufère, M. Raynal, G. Dibarboure, and M. Picot (2018). Gauging the improvement of recent means ea surface models: A new approach for identifying and quantifying this errors, *Journal of Geophysical Research, Oceans*, 123, 5889-5911, doi: 101029/2017JC013503.

Pujol, M.-I., Faugère, Y., Taburet, G., Dupuy, S., Pelloquin, C., Ablain, M., and Picot, N. (2016). DUACS DT2014: The new multi-mission altimeter data set reprocessed over 20 years. *Ocean Science*, 12(5), 1067–1090, doi: 10.5194/os-12-1067-2016.

Purich, A., England, M. H., Cai, W., Sullivan, A., and Durack, P. J. (2018). Impacts of broad-scale surface freshening of the Southern Ocean in a coupled climate model. *Journal of Climate*, 31(7), 2613– 2632. doi: 10.1175/JCLI-D-17-0092.1

Rio, M.-H., S. Mulet, and N. Picot (2014), Beyond GOCE for the ocean circulation estimate: synergetic use of altimetry, gravimetry, and in situ data provides new insight into geostrophic and Ekman currents, *Geophysical Research Letters,* 41, doi:10.1002/2014GL061773.

731 Romero, S. I., A.R. Piola, M. Charo, and C. A. E. Garcia (2006). Chlorophyll-a variability off
732 Patagonia based on SeaWiFS data. *Journal of Geophysical Research, Oceans*, 111,
733 C05021, doi: 10.1029/2005JC003244.
734 Saraceno, M., C. Provost, and A.R. Piola (2005). On the relationship between satellite-retrieved
735 surface temperature fronts and chlorophyll a in the western South Atlantic. *Journal of*
736 *Geophysical Research, Oceans*, 110(C11), doi: 10.1029/2004JC002736.
737 Schmid, C. (2014). Mean vertical and horizontal structure of the subtropical circulation in the
738 South Atlantic from three-dimensional observed velocity fields. *Deep Sea Research Part*
739 *I: Oceanographic Research Papers*, 91, 50-71, doi: 10.1016/j.dsr.2014.04.015.
740 Spadone A. and C. Provost, (2009). Variations in the Malvinas Current volume transport since
741 October 1992, *Journal of Geophysical Research, Oceans*, 114, C02002,
742 doi:10.1029/2008JC004882.
743 Smith, W. H. F., and D. T. Sandwell (1994), Bathymetric prediction from dense satellite
744 altimetry and sparse shipboard bathymetry, *Journal of Geophysical Research*, *Solid*
745 *Earth*, 99, 21 803–21 824, doi: 10.1029/94JB00988.
746 Szekeley, T., J. Gourrion, S. Pouliquen, and G. Reverdin (2016). CORA, Coriolis, Ocean
747 Dataset for Reanalysis. SEANOE, doi:10.1029/2008JC05248
748 Valla, D., A.R. Piola, C. S. Meinen, and E. Campos (2018). Strong mixing and recirculation in
749 the northwestern Argentine Basin. *Journal of Geophysical Research, Oceans*, 123(7),
750 4624-4648, doi:10.1029/2018JC013907.
751 Valla, D. and A.R. Piola (2015). Evidence of upwelling events at the northern Patagonian shelf
752 break. *Journal of Geophysical Research, Oceans*, 120, 7635–7656,
753 doi:10.1002/2015JC011002.

754 Vivier F. and C. Provost, (1999a). Direct velocity measurements in the Malvinas Current.
755 *Journal of Geophysical Research, Oceans*, 104, 21083-21104, doi:
756 10.1029/1999JC900163.
757 Vivier F. and C. Provost, (1999b). Volume Transport of the Malvinas Current: Can the flow be
758 monitored by TOPEX/Poseidon? *Journal of Geophysical Research, Oceans*, 104, 21105-
759 21122, doi: 10.1029/1999JC900056.
760 Vivier F., C. Provost and M. P. Meredith (2001). Remote and local wind forcing in the
761 Brazil/Malvinas Region. *Journal of Physical Oceanography*, 31, 892-913, doi:
762 10.1175/1520-0485.
763 Wu, L., W. Cai., L. Zhang, H. Nakamura, A. Timmermann, T. Joyce, J. M. McPhaden, M.
764 Alexander, B. Qiu, M. Visbeck, P. Change and B. Giese (2012). Enhanced warming over
765 the global subtropical western boundary currents. Nature Climate Change, 2(3), 161, doi:
766 10.1038/nclimate1353
767 Yang, H., G. Lohmann, W. Wei, M. Dima, M. Ionita and J. Liu. (2016). Intensification and
768 poleward shift of subtropical western boundary currents in a warming climate. *Journal of*
769 *Geophysical Research: Oceans*, 121(7), 4928-4945. doi: 10.1002/2015JC011513

Figure captions:

Figure 1: Mean surface velocity and eddy kinetic energy from 25 years of ocean reanalysis (1993-2017): (a-c) Mean surface velocity magnitude (in cm/s) and mean surface velocity vectors (when larger than 10 cm/s) and (b-d) mean surface eddy kinetic energy per unit mass (in cm^2/s^{-2}). The black, cyan and red contours represent the mean position of the Subantarctic Front (SAF), Subtropical Front (STF) and the Polar Front (PF) and are respectively defined as contours of model SSH values of 5, 40 and -40 cm as in Artana et al. (2018b). In the upper panels (c and d) 3 sections are indicated in purple: one across the MC at 41°S, one across the BC at 36°S and one following approximately the 2,000 m isobath. Bottom topography isobaths (from Smith and Sandwell, 1994) in a, b, c and d correspond to 6000, 5000, 3000, 2000, 1000 and 300 m. The spatial distribution of current meters from the successive arrays is indicated with red 2014-2015, black 2001-2003 and green 1993-1995 diamonds in d. Mean wind stress curl (e) and zonal wind stress (f) from 25 years of Era-Interim reanalysis. The black thick contours in each field represent the mean position of the zero isoline. The mean position of the zero isoline of the zonal wind stress for the summer (winter) is indicated with the red (blue) contour in panel f.

Figure 2: Model mean vertical structure of the (a) along slope velocities (V// in cm/s), (b) across slope velocities ($V\perp$ in cm/s), (c) vertical velocities (w in m/day), (d) potential temperature (θ in °C), (e) salinity (S in psu) and (f) potential density (σ in kg/m^3) over the period 1993-2017 and along 3 sections: (I) The MC section at 41°S, (II) a section following the 2,000 m isobath and (III) the BC section at 36°S. The thick black and red vertical line indicate the mean position of the SAF and STF over the period 1993-2017. The X axis is distance in km and the Y axis is depth in m. The thin black vertical lines indicate the intersection of the MC

794 and BC sections with the 2,000 m isobath. In f the 27.16 kg/m^3 and 26.95 kg/m^3 isopycnals are
795 indicated with dashed black contours.
796
797 **Figure 3:** Model std vertical structure of the (a) along slope velocities (V// in cm/s), (b) across
798 slope velocities (V⊥ in cm/s), (c) vertical velocities (w in m/day), (d) potential temperature (θ
799 in °C), (e) salinity (S in psu) and (f) potential density (σ in kg/m^3) over the period 1993-2017
800 and along 3 sections: (I) The MC section at 41°S, (II) a section following the 2,000 m isobath
801 and (III) the BC section at 36°S. The X axis is distance in km and the Y axis is depth in m. The
802 thick black and red vertical line indicate the mean position of the SAF and STF over the period
803 1993-2017. The thin black vertical lines indicate the intersection of the MC and BC sections
804 with the 2,000 m isobath.
805
806 **Figure 4:** std associated with the seasonal cycle for the (a) along slope velocities (V// in cm/s),
807 (b) across slope velocities (V⊥ in cm/s), (c) vertical velocities (w in m/day), (d) potential
808 temperature (θ in °C), (e) salinity (S in psu) and (f) potential density (σ in kg/m^3) over the
809 period 1993-2017 and along 3 sections: (I) The MC section at 41°S, (II) a section following the
810 2,000 m isobath and (III) the BC section at 36°S. The X axis is distance in km and the Y axis
811 is depth in m. The thick black and red vertical line indicate the mean position of the SAF and
812 STF over the period 1993-2017. The thin black vertical lines indicate the intersection of the
813 MC and BC sections with the 2,000 m isobath. For sake of comparison we kept the same scale
814 as in Figure 3.
815
816 **Figure 5:** 2,000 m isobath section: Dominant joint EOF of model velocity (along and across
817 slope components) and potential density field (30 % of the total variance). (a) Time series
818 associated with EOF-1. Red horizontal lines indicate the mean and 1.5 standard deviation on

819 each side of the mean. (b) EOF-1 of joint model along and across slope velocities and potential
820 density. (c) Mean model along and across slope velocities (in cm/s) and potential density
821 structure (in kg/m^3) of the 2,000 m isobaths section. (d) Positive phase of EOF-1 computed
822 adding the mean field from (c) to the EOF-1 structure from (b) multiplied by 1.5 the standard
823 deviation from (a): Mean (c)+ EOF-1 (b) *1.5std (EOF-1) (a). (e) Negative phase of EOF-1:
824 Mean (c) EOF-1 (b)*1.5 std (EOF-1) (a). The X axis is distance in km and the Y axis is depth
825 in m. The dashed white line in the potential density field of EOF+ and EOF- indicates the mean
826 position of the 27.1 kg/m^3 isopycnal. The location of the 27.16 kg/m^3 and 26.95 kg/m^3
827 isopycnals (black dashed lines in the potential density fields) at 500 m depth (black horizontal
828 line) define the position of the SAF (black vertical line) and STF (red vertical line). The thin
829 black vertical lines indicate the intersection of the MC and BC sections with the 2,000 m
830 isobath.
831
832 **Figure 6:** Model snapshot on March 19, 2015. Model salinity maps and velocity at the surface
833 (a), 100 m (b) and 500 m (c). Only velocities larger than 15 cm/s are represented. The SAF and
834 STF from model SSH are indicated in gray and red in (a) and (b). Model synoptic vertical
835 structure of the (d) along slope velocities (V// in cm/s), (e) salinity (S in psu), (f) potential
836 density (σ in kg/m^3) and (g) vertical velocities (w in m/day) along 3 sections: the MC section
837 at 41°S (I), the section following the 2,000 m isobath (II) and the BC section at 36°S (III). The
838 X axis is distance in km and the Y axis is depth in m. The thick gray and red vertical lines
839 indicate the instantaneous position of the SAF and STF. The thin gray and red vertical lines
840 indicate the mean position of the SAF and STF over the period 1993-2017. The thin vertical
841 black lines indicate the intersection of the MC and BC sections with the 2,000 m isobath. The
842 black dot indicates the location of the time series shown in Figure 7.
843

844 **Figure 7:** Time series of along-slope velocities in panel a, and temperature (red) and salinity
845 (blue) in panel b at 763 m depth at km 40 of the 36°S BC section (black dot in Figure 6 III d).
846 A horizontal blue line marks the mean for each variable.
847
848 **Figure 8:** (a) Mean surface geostrophic velocities (MSGV) from CNES-CLS13 and CNES-
849 CLS18 mean dynamic topography. The dots represent the mean surface velocity at the mooring
850 position from the LUT-iterative method. The dashed line is the mean surface velocity profile
851 used in the LUT. (b) MC volume transport in Sv computed with the LUT method in the upper
852 1,500 m (blue) and model outputs in the upper 900 m (magenta). The *in-situ* measurements
853 periods are indicated in colors. (c) Yearly averages of the MC LUT (in bleu) and model (in
854 magenta) transport in the upper 1,500 m from January 1993 to December 2017. Red, green and
855 black colored bars indicated in situ observations periods (1993-1995, 2001-2003 and 2014-
856 2015). The magenta horizontal line marks the mean model transport for the 1993-2017. (d)
857 Variance preserving spectra of the LUT (blue) and model (magenta) MC volume transport. The
858 dotted line shows the 90% confidence level against the red noise background from a first-order
859 autoregressive process (e) wavelet transform of the model MC transport time series. The
860 wavelet amplitude is shown in base 2 logarithm. The black lines indicate the 90% confidence
861 level.
862
863 **Figure 9:** (a) MC (blue) and BC (red) volume transport in Sv at 41°S and 36°S computed from
864 model outputs in the upper 900 m. (b) Yearly averages of the model BC transport in the upper
865 900 m from January 1993 to December 2017. The standard deviation is shown by the blue line
866 centered on each bar. The black horizontal line marks the mean transport for the 1993-2017.
867 (c) Variance preserving spectrum of the BC volume transport. The dotted line shows the 90%
868 confidence level against the red noise background from a first-order autoregressive process (d)

wavelet transform of the model BC transport time series. The wavelet amplitude is shown in base 2 logarithm. The black lines indicate the 90% confidence level.

Figure 10: (a) Model SSH along the 2,000 m isobath. The Y-axis is distance from 42°S 56.75°W. X axis is time (in years). The 5 and 40 cm SSH values corresponding to the SAF and STF are marked with white and purple, respectively. Year 2015 is outlined in between vertical white dashed lines. The white and purple horizontal lines represent the mean position of the SAF and STF front over the period 1993-2017. (b) Close up of (a) over year 2015. The thin black horizontal lines represent the intersection of the MC and BC sections with the 2,000 m isobath. The thick purple and white lines indicate the mean position of the SAF and STF position. (c) Model MC at 41°S and BC at 36°S and 37°S volume transport time series for year 2015. The horizontal lines indicate the mean and 1.5 std on each side of the mean. (d) Wind stress curl above the 2,000 m isobath for the year 2015 with the SAF and STF isolines (white and purple) surperimposed.

Figure 11: (a) Monthly mean position of the STF and SAF defined with model SSH isolines 5 and 40 cm isolines respectively. (b) Monthy mean distance between the SAF and STF. The red line indicates the mean distance over the period 1993-2017. (c) Monthly mean STF and SAF positions on the 2,000 m isobath with MC and BC monthly mean transport superimposed. (d) Monthly mean position of the zero isoline of the zonal component of the wind stress over a section following the 2,000 m isobath (magenta line in Figure 1 f).

Figure 12: Mean annual position of the STF (a) and SAF (b) defined with model SSH isolines 5 and 40 cm isolines respectively. (c) Mean annual distance between the SAF and STF. The red line indicates the mean annual distance averaged over the period 1993-2017. (d) annual mean

894 STF and SAF positions on the 2,000 m isobath with MC and BC annual transport superimposed.
895 (e) Annual mean position of the zero isoline of the zonal component of the wind stress over a
896 section following the 2,000 m isobath (magenta line in Figure 1 f).
897
898 **Figure 13:** Linear trends over the 25 years for the (a) along slope velocities (V// in cm/s/years),
899 (b) across slope velocities (V⊥ in cm/s/year) (c) potential temperature (θ in °C/year), (d) salinity
900 (S in psu/year) and (e) potential density (σ in kg/m^3/year) over the period 1993-2017 and along
901 3 sections: (I) The MC section at 41°S, (II) a section following the 2,000 m isobath and (III)
902 the BC section at 36°S. (f) Potential density field (in kg/m^3) obtained after adding the trend (e)
903 to the mean field (Figure 2 e). The X axis is distance in km and the Y axis is depth in m. In each
904 panel the thin black and red vertical line indicate the mean position of the SAF and STF over
905 the period 1993-2017. The thick black and red vertical lines indicate the position of the position
906 of the SAF and STF deduced from 27.16 kg/m^3 and 26.95 kg/m^3 at 541 m (dashed black
907 isolines) in f: the two fronts moved southward, the SAF by 50 km and the STF by 150 km.
908
909
910
911
912
913
914
915
916
917
918

Figures:

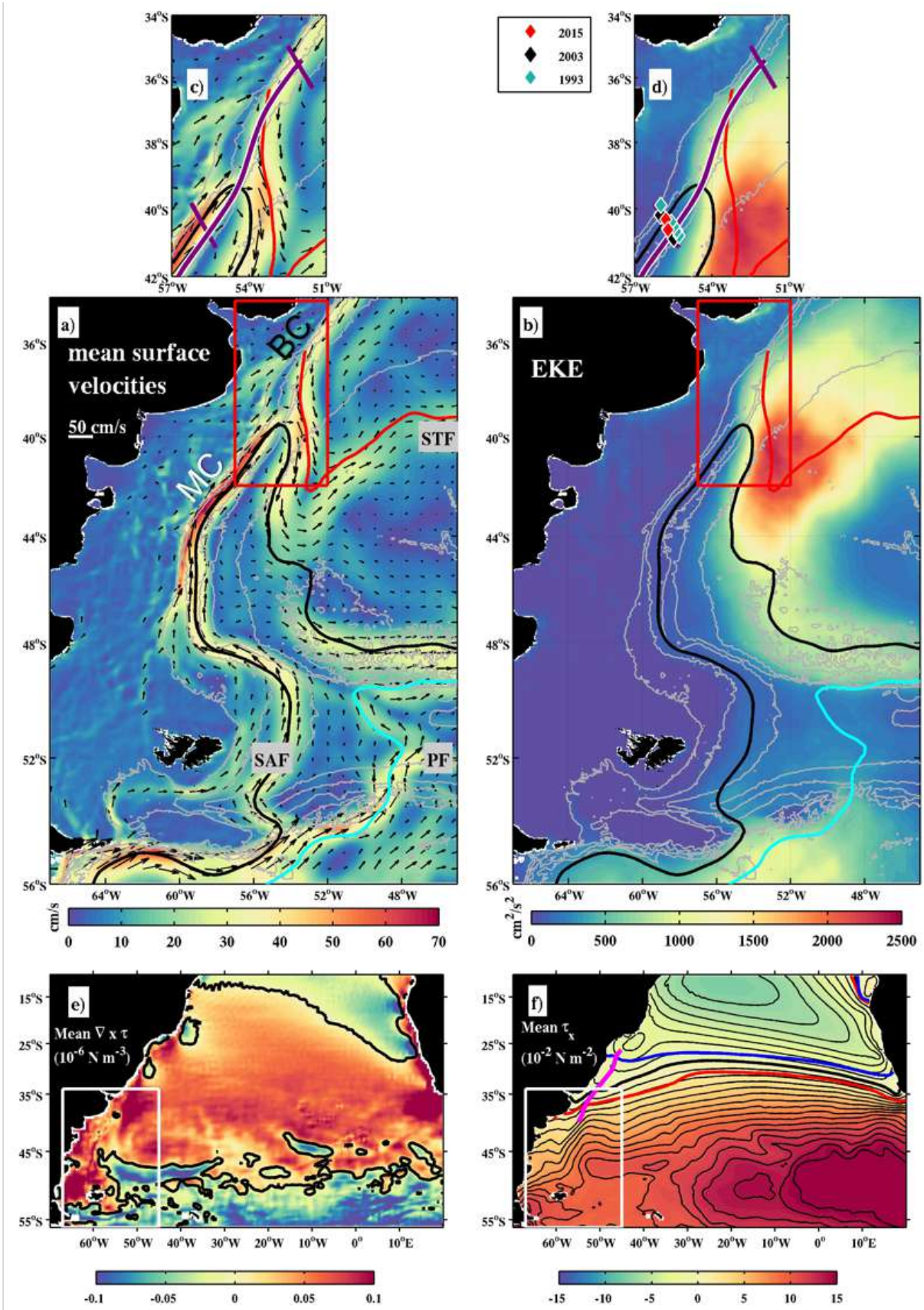

Figure 1

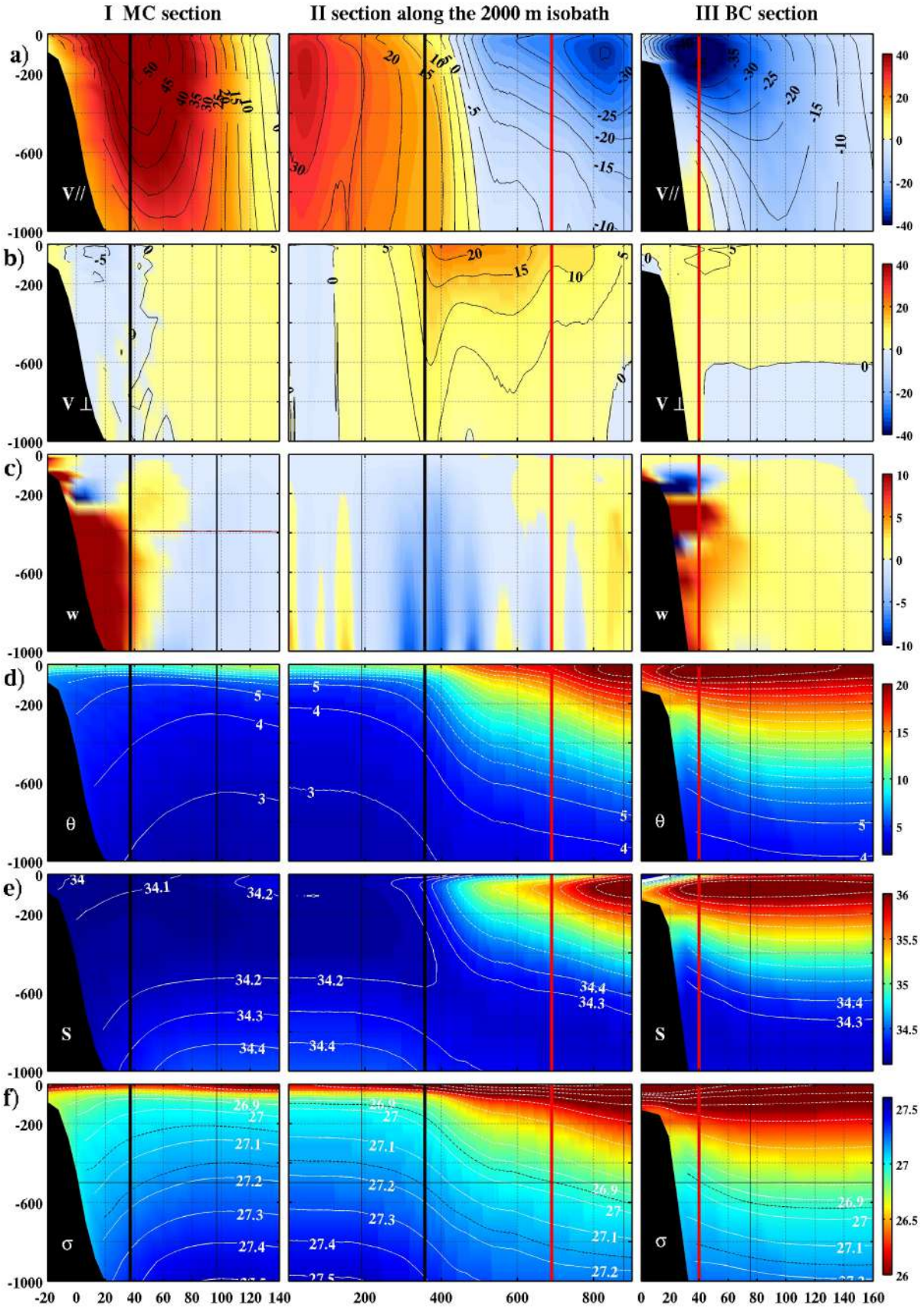
I MC section
II section along the 2000 m isobath
III BC section
a)
b)
c)
d)
e)
f)
V//
V⊥
w
θ
S
σ

Figure 2

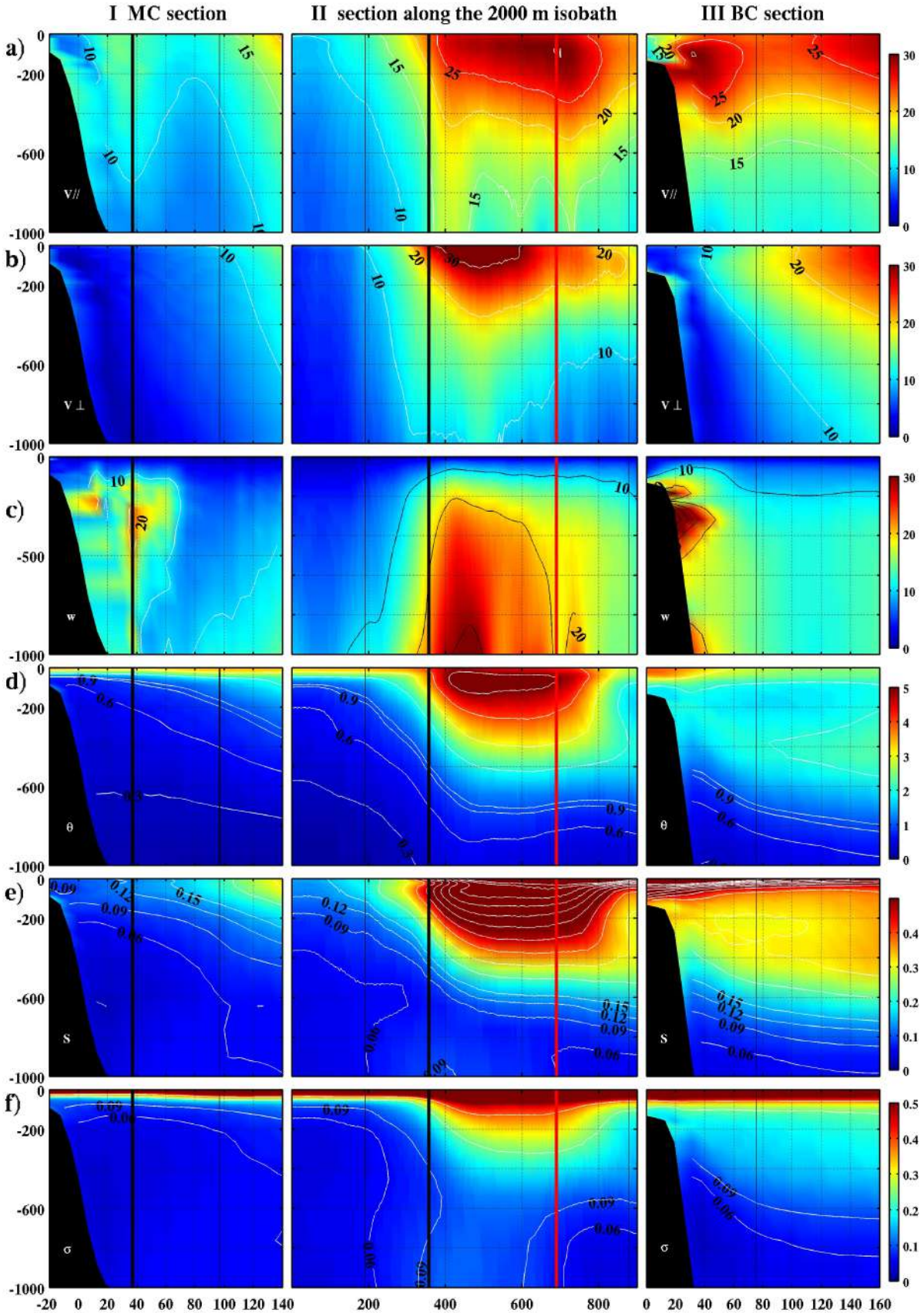
I MC section
II section along the 2000 m isobath
III BC section
a)
b)
c)
d)
e)
f)
V//
V⊥
w
θ
S
σ

Figure 3

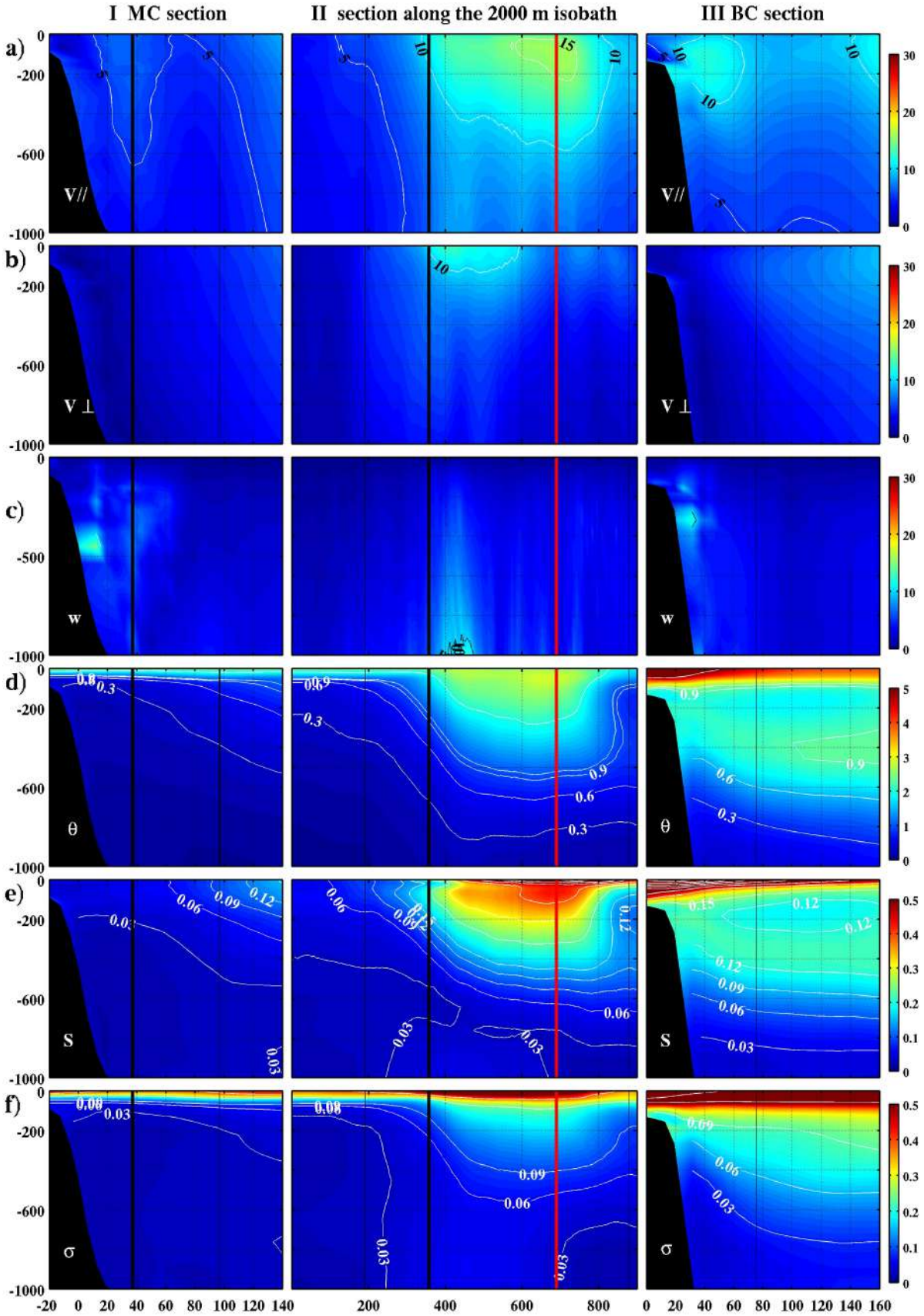
I MC section
II section along the 2000 m isobath
III BC section
a)
b)
c)
d)
e)
f)
V//
V⊥
w
θ
S
σ

Figure 4

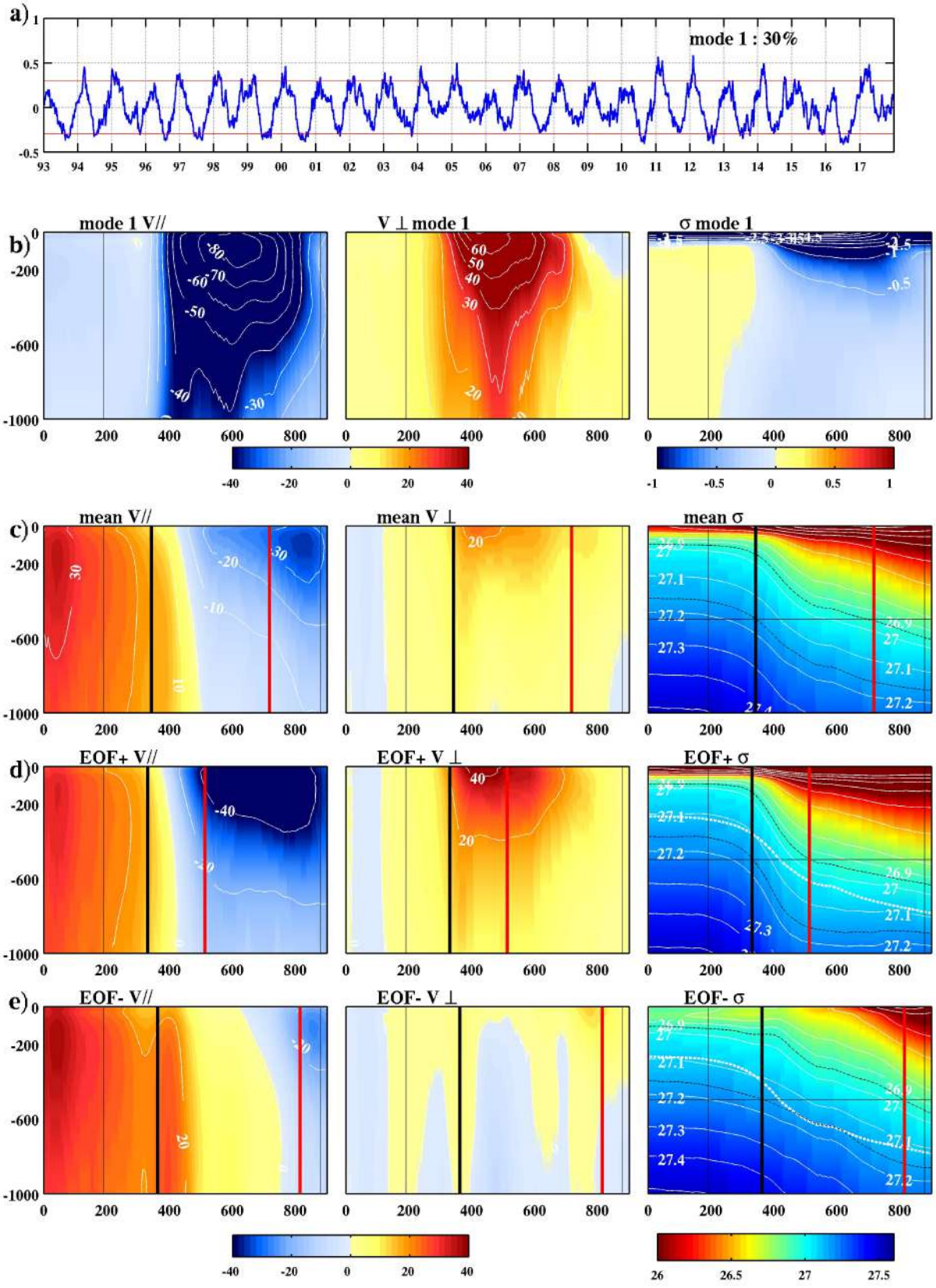

932
933 Figure 5

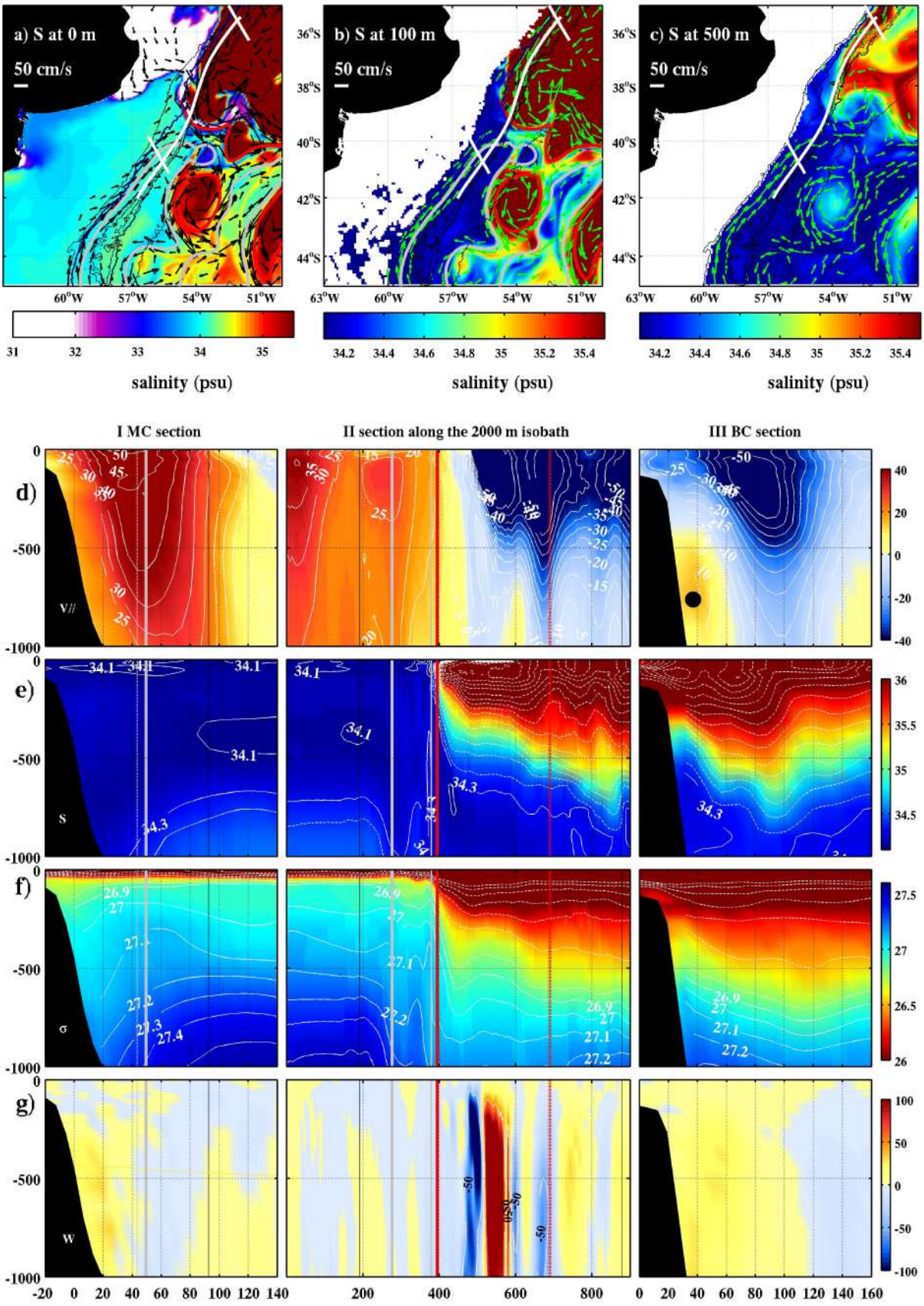
a) S at 0 m
50 cm/s
b) S at 100 m
50 cm/s
c) S at 500 m
50 cm/s
salinity (psu)
salinity (psu)
salinity (psu)
I MC section
II section along the 2000 m isobath
III BC section
d)
e)
f)
g)
V//
S
σ
W

Figure 6

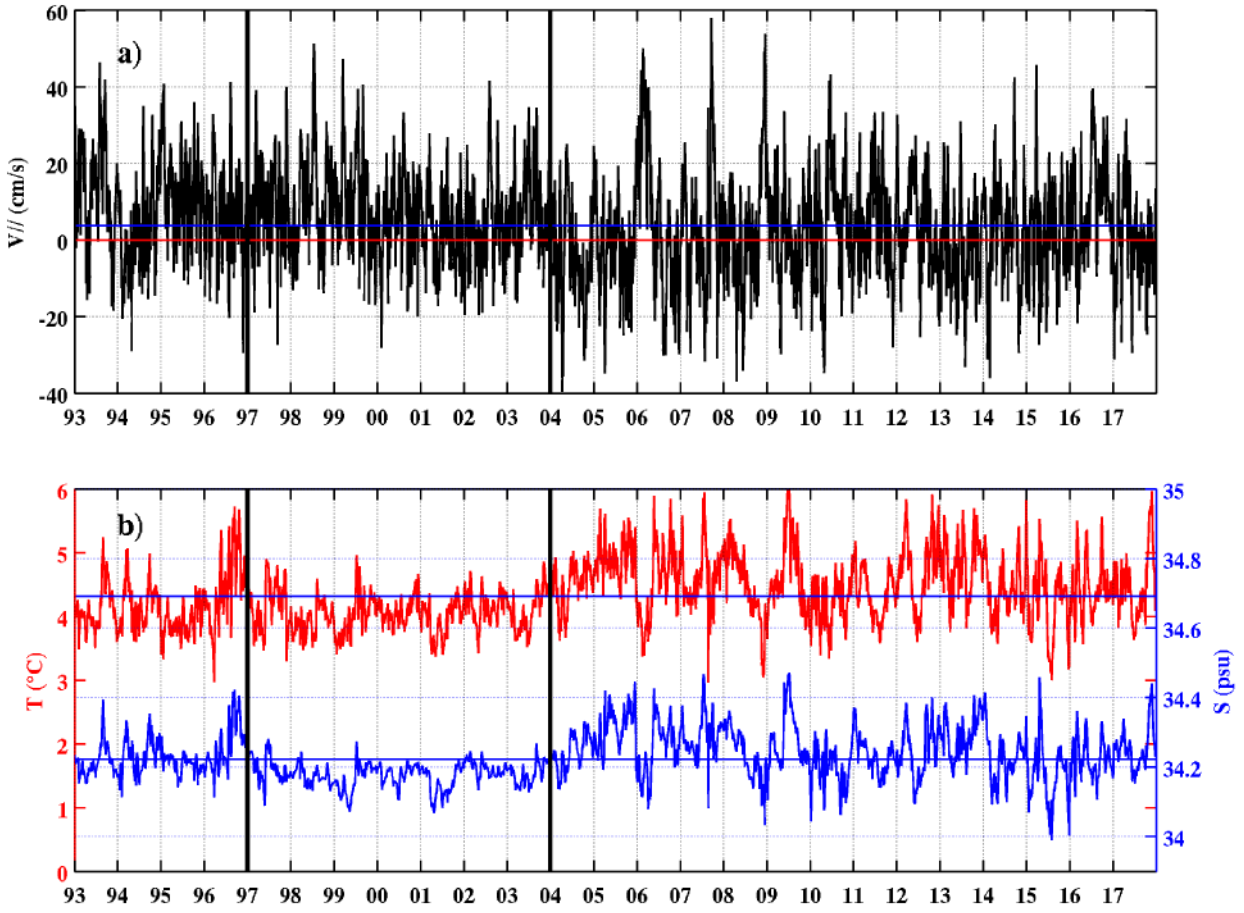
a)
V// (cm/s)
60
40
20
0
-20
-40
93 94 95 96 97 98 99 00 01 02 03 04 05 06 07 08 09 10 11 12 13 14 15 16 17
b)
T (°C)
S (psu)
6
5
4
3
2
1
0
35
34.8
34.6
34.4
34.2
34
93 94 95 96 97 98 99 00 01 02 03 04 05 06 07 08 09 10 11 12 13 14 15 16 17

Figure 7

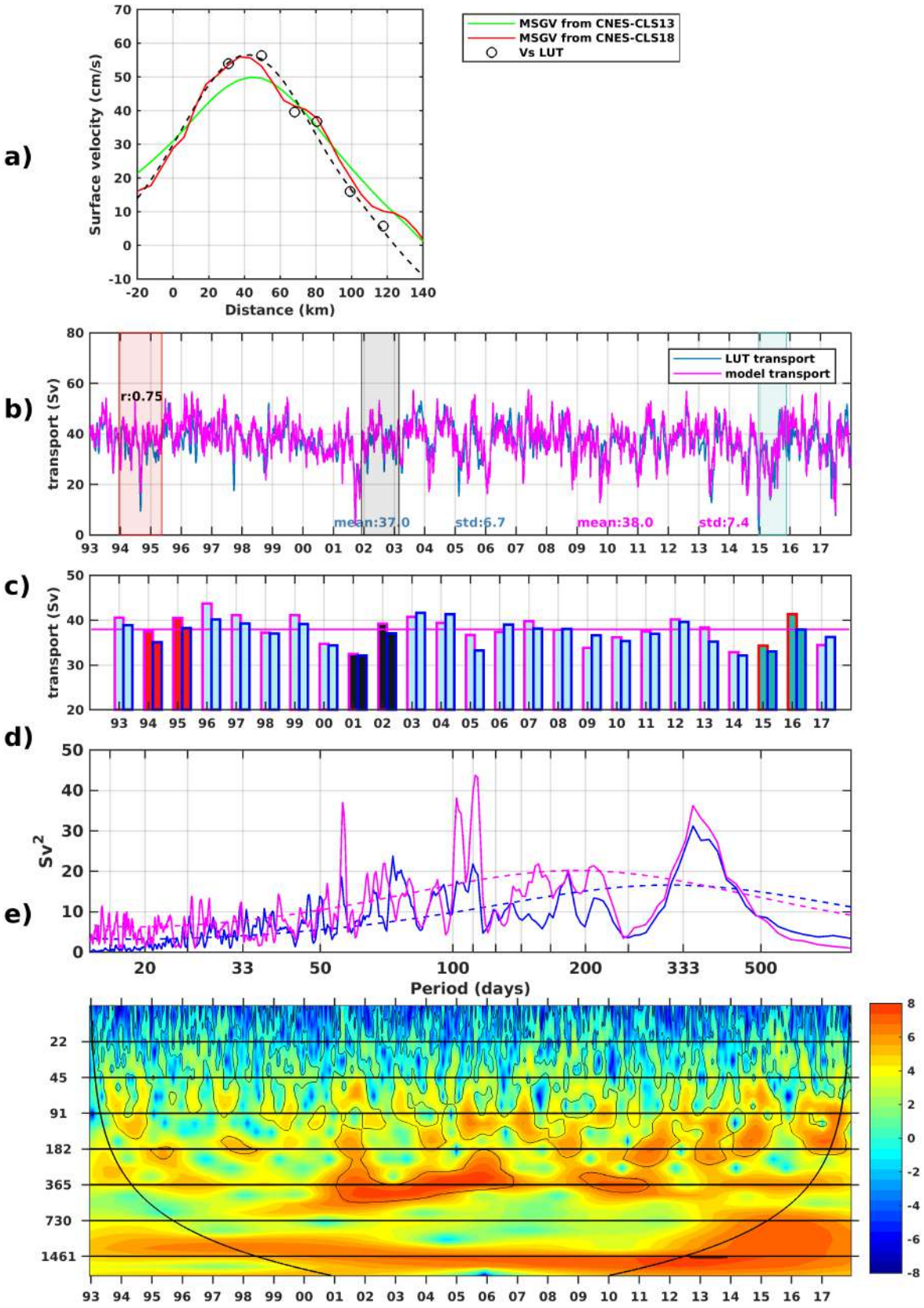

940
941 Figure 8
942

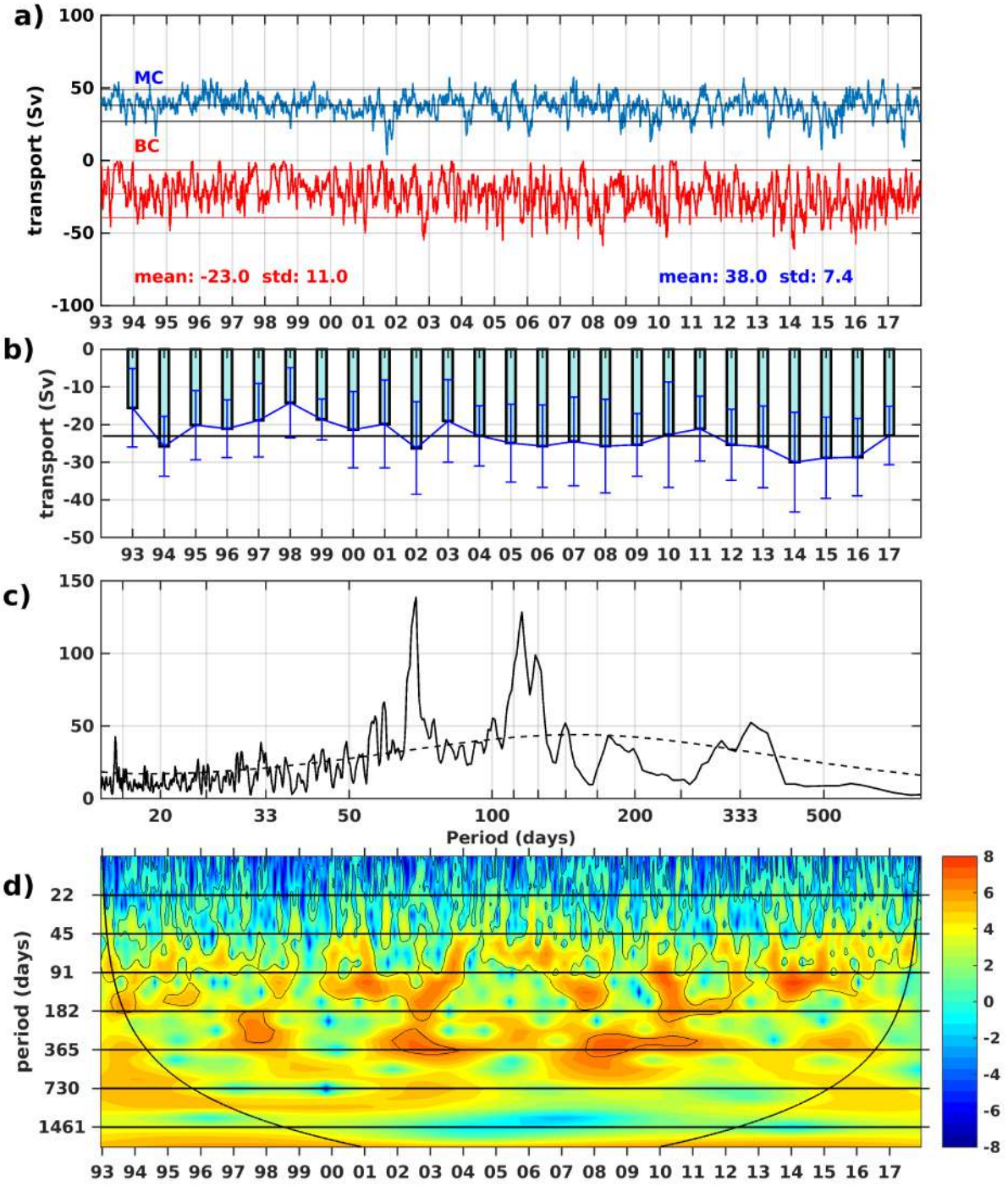
a)
MC
BC
transport (Sv)
mean: -23.0 std: 11.0
mean: 38.0 std: 7.4
b)
transport (Sv)
c)
Period (days)
d)
period (days)
93 94 95 96 97 98 99 00 01 02 03 04 05 06 07 08 09 10 11 12 13 14 15 16 17

Figure 9

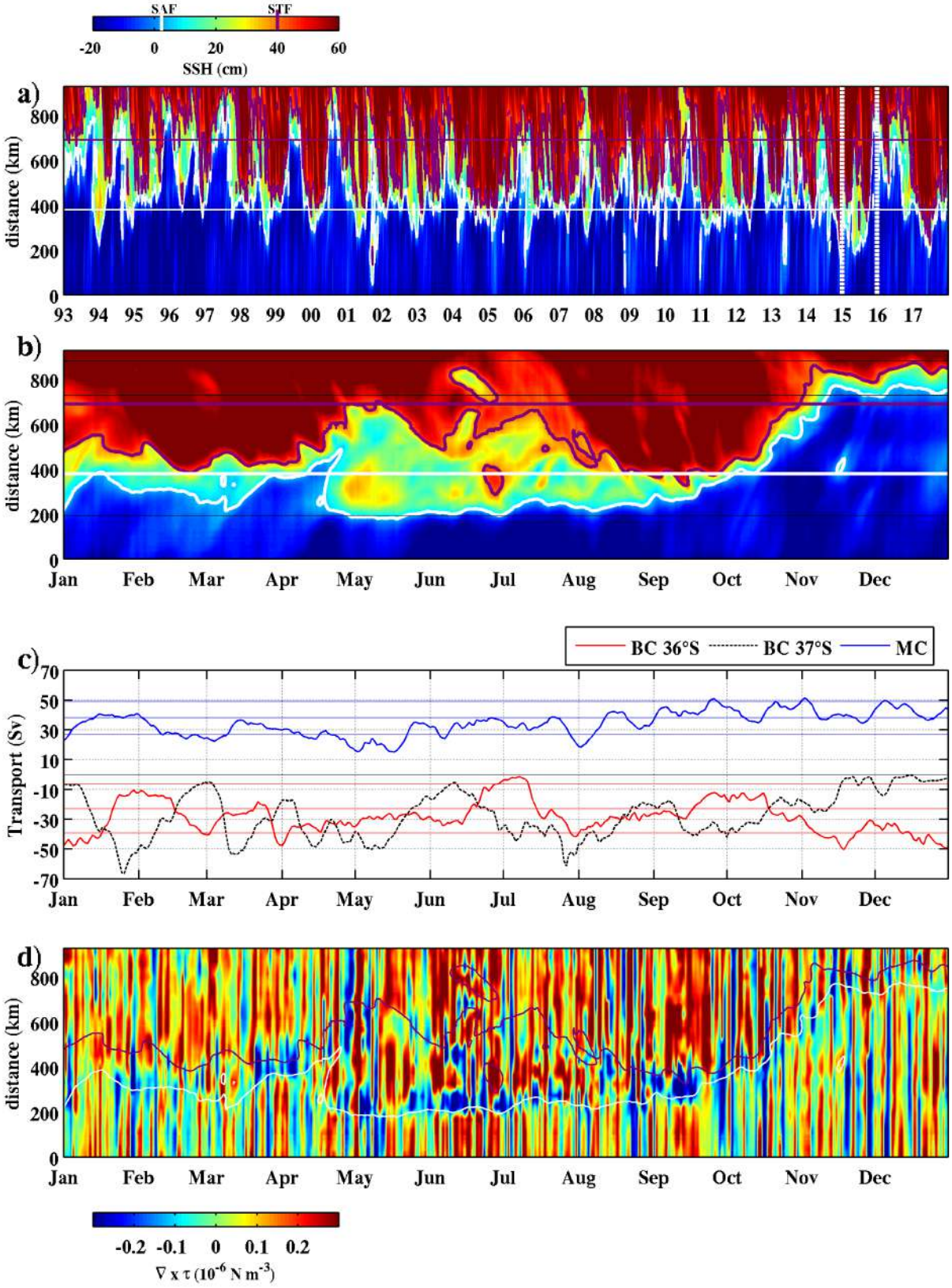

945
946 Figure 10
947

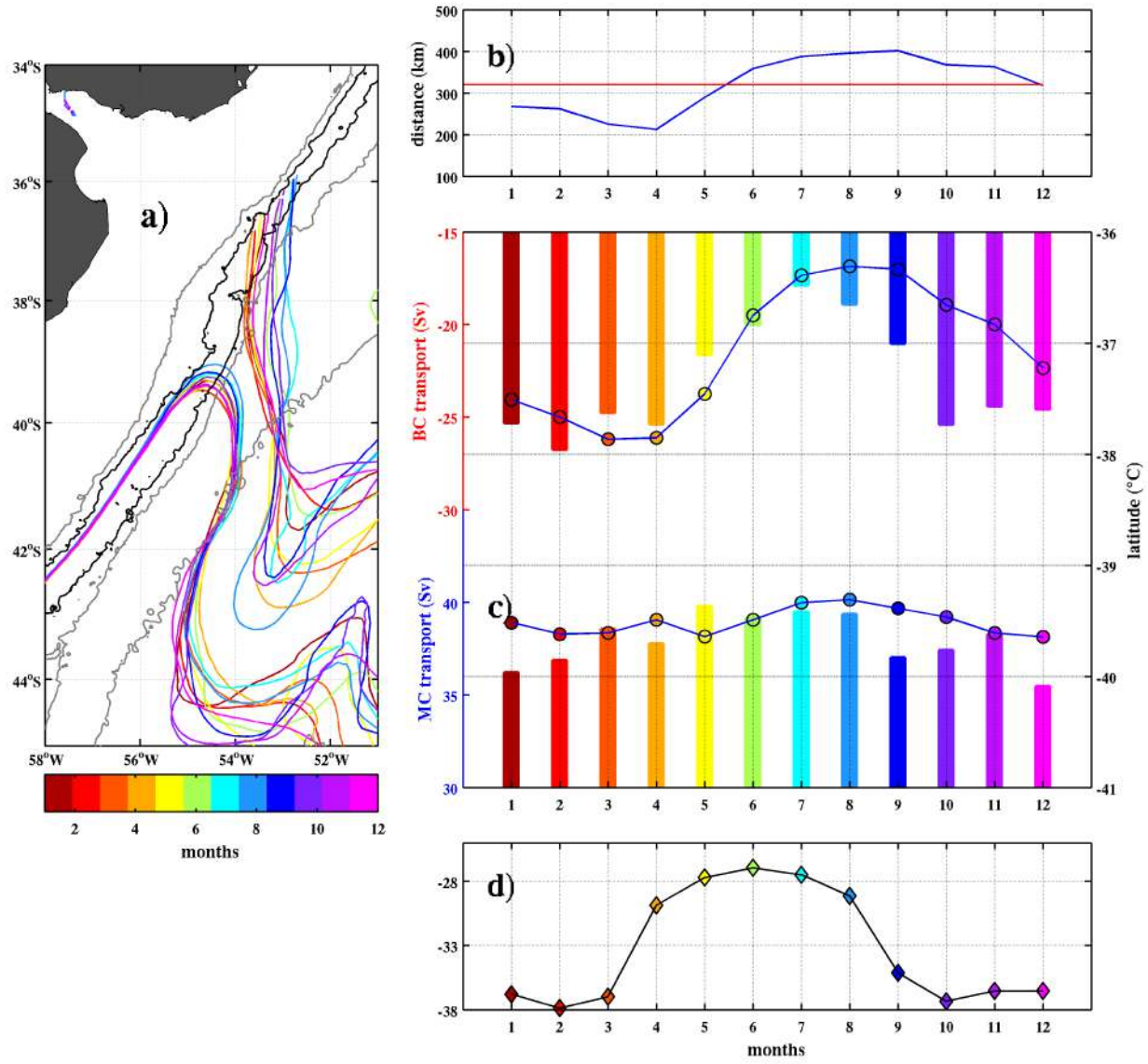
a)
b)
c)
d)
34°S
36°S
38°S
40°S
42°S
44°S
58°W
56°W
54°W
52°W
2
4
6
8
10
12
months
distance (km)
500
400
300
200
100
1
2
3
4
5
6
7
8
9
10
11
12
BC transport (Sv)
-15
-20
-25
-30
MC transport (Sv)
40
35
30
latitude (°C)
-36
-37
-38
-39
-40
-41
-28
-33
-38
months

Figure 11

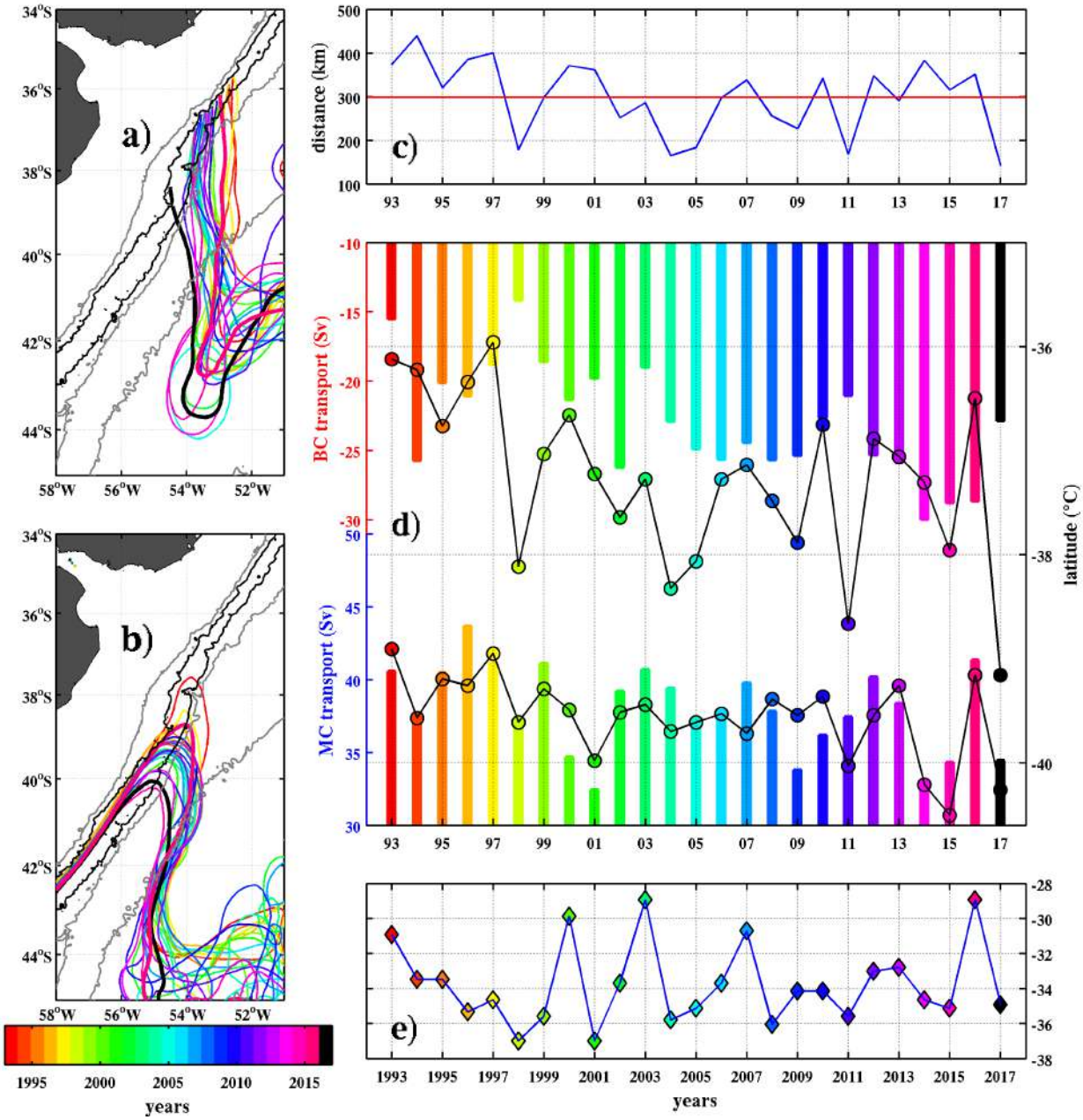
a)
b)
c)
d)
e)
34°S
36°S
38°S
40°S
42°S
44°S
58°W
56°W
54°W
52°W
1995
2000
2005
2010
2015
years
distance (km)
BC transport (Sv)
MC transport (Sv)
latitude (°C)
1993
1995
1997
1999
2001
2003
2005
2007
2009
2011
2013
2015
2017

Figure 12

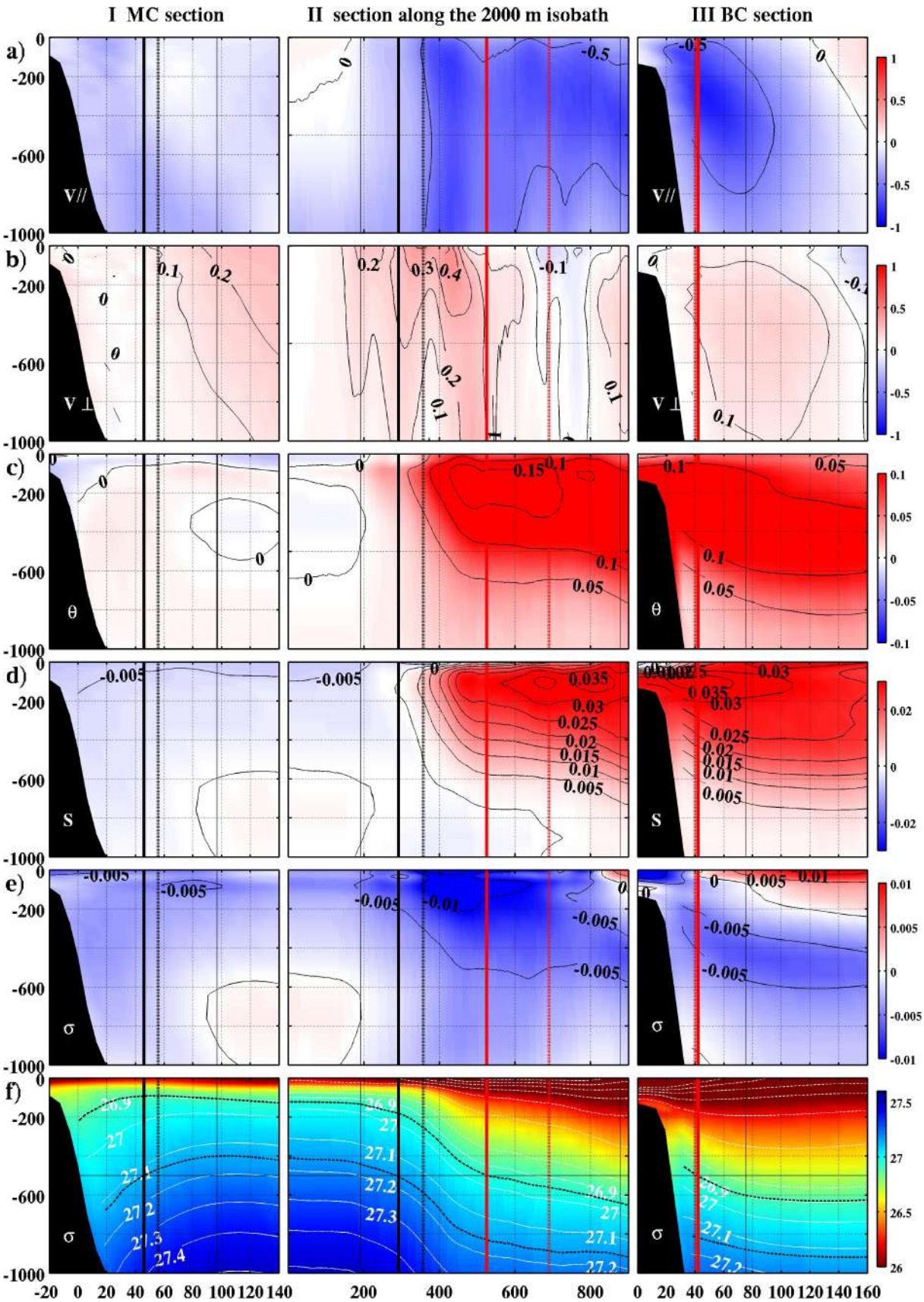
I MC section
II section along the 2000 m isobath
III BC section
a)
b)
c)
d)
e)
f)
V//
V⊥
θ
S
σ
σ
-1000
-600
-200
0
-20 0 20 40 60 80 100 120 140
200 400 600 800
0 20 40 60 80 100 120 140 160

Figure 13